AIMS Mathematics

http://www.aimspress.com/journal/Math

AIMS Mathematics, 11(11): 38451–38491.
DOI: 10.3934/math.20261485
Received: 22 July 2026
Revised: 28 October 2026
Accepted: 13 November 2026
Published: 18 November 2026

Research article

Delay-induced four-phase rotating waves and numerical brackets for stochastic P- and D-transitions in a four-oscillator central pattern generator

Qiyuan He[1], Chonghe Shi[2], Zikun Han[3] and Qiubao Wang[1,*]

[1] Department of Mathematics and Physics, Shijiazhuang Tiedao University, Shijiazhuang, Hebei 050043, China

[2] School of Mechanical Engineering, Shijiazhuang Tiedao University, Shijiazhuang, Hebei 050043, China

[3] Department of Engineering Mechanics, Shijiazhuang Tiedao University, Shijiazhuang, Hebei 050043, China

* **Correspondence:** Email: wangqiubao12@sina.com.

Abstract: Time delay can select coordinated rhythms in central pattern generator networks, but deterministic existence does not ensure robustness under stochastic perturbations. We investigate a four-oscillator Stuart–Landau ring with delayed unidirectional coupling and multiplicative Itô noise. The original deterministic delay differential equation identifies a critical spatial mode with adjacent phase differences of $\pi/2$. A stochastic Galerkin–Koornwinder approximation converts the infinite-dimensional delay system into finite-dimensional systems for spectral, continuation, and stochastic analyses. Periodic continuation and Floquet multipliers reveal a bounded delay interval supporting a stable four-phase rotating wave, namely, a quarter-cycle pattern with adjacent phase differences of $\pi/2$. For the full $N = 8$ approximation, long-time simulations yield sampled phenomenological (P) transition brackets, identified by the change from an interior amplitude-density peak to boundary dominance, and dynamical (D) transition estimates, determined from the local sample stability of the absorbing zero state, which represents the loss of rhythmic CPG output as oscillation amplitudes decay to zero. Across the sampled delays, the P transition precedes the D transition, producing an intermediate regime in which the most probable nonzero amplitude has disappeared although the zero state is not yet locally sample stable. Representative $N = 9$ and $N = 10$ calculations provide directional truncation checks, while multi-seed, time-window, and step-size tests quantify numerical sensitivity of the D boundary. Combining the deterministic periodic window, stochastic transition brackets, and phase-performance diagnostics gives candidate finite-order operating intervals and identifies $\tau = 2.35$ as the grid point with the largest sampled joint margin. These transition boundaries are numerical results for the finite-order approximation rather than direct boundaries of the original stochastic delay equation.

Keywords: central pattern generator; Stuart–Landau oscillator; delay differential equation; quarter-

cycle rotating wave; stochastic Galerkin–Koornwinder approximation; P-bifurcation; D-bifurcation; multiplicative noise
Mathematics Subject Classification: 34K18, 34K50, 37H20, 37M20, 65C30

Abbreviations:
CPG, central pattern generator;
DDE, delay differential equation;
SDDE, stochastic delay differential equation;
SGK, stochastic Galerkin–Koornwinder approximation;
KDE, kernel density estimation.

1. Introduction

Quadruped robots can exploit discrete footholds to traverse discontinuous terrain and are therefore attractive for inspection, rescue, and field transportation. Their locomotion, however, requires the coordinated generation of rhythmic signals, prescribed phase relations among the legs, and stability of the resulting periodic motion. These questions can be naturally formulated within nonlinear dynamics, where robotic gaits are represented by periodic or phase-locked solutions with specific spatiotemporal symmetries [1]. Central pattern generators (CPGs) provide a compact mechanism for producing such rhythms, and networks of coupled nonlinear oscillators have consequently been used to coordinate the amplitudes, frequencies, and phases of legged locomotion [2–5]. For four-node CPG networks, gait selection is closely related to the symmetry and phase structure of the critical oscillatory mode. In this article, a rotating state with four sequential phases and adjacent phase differences of $\pi/2$ is termed a four-phase, or quarter-cycle, rotating wave. In particular, symmetry-breaking and phase-oscillator analyses have linked quarter-cycle phase shifts to quadrupedal gait patterns [6, 7].

Time delay is unavoidable in sensing, communication, controller computation, and actuator response, but it need not act solely as a detrimental factor; it can also serve as a bifurcation parameter for regulating oscillation frequency and phase relations. Delay-coupled oscillator networks can generate prescribed rotating waves and locomotion rhythms through Hopf bifurcation, thereby replacing purely trial-and-error tuning with dynamical conditions for the existence of target phase patterns [8–10]. Related delay-induced Hopf analyses demonstrate how characteristic equations, center-manifold reduction, and normal-form calculations connect a critical delay to the onset and stability of periodic solutions [11]. These studies clarify the deterministic connection among coupling delay, critical spatial modes, and oscillation generation. The existence and Floquet stability of a deterministic periodic solution, however, do not establish robustness under random perturbations. Foot–ground impacts, payload variations, actuator errors, and parameter fluctuations may perturb both amplitude and phase, causing degradation of the rhythmic output or even extinction of the oscillation.

Stochastic bifurcation theory provides two complementary descriptions of noise-induced qualitative changes. A phenomenological, or P-bifurcation, is associated with a change in the extremum structure of a stationary probability density, whereas a dynamical, or D-bifurcation, concerns changes in sample stability or invariant random states [12]. Recent studies have also used top Lyapunov exponents and invariant probability measures to distinguish noise-dependent persistence and extinction regimes

in stochastic dynamical systems [13]. In stochastic delayed systems, noise may shift deterministic bifurcation thresholds, alter stationary amplitude distributions, induce stabilization or destabilization [14, 15], and generate more complex delay-dependent stochastic dynamics [16]. Studies of delayed networks and feedback-controlled oscillators further show that the P- and D-bifurcation boundaries need not coincide and may provide distinct parameter-selection criteria [17–19]. For a gait-generating CPG, these criteria answer different questions: whether a nonzero rhythmic amplitude remains the most probable state, and whether the absorbing zero state becomes sample-exponentially stable. Their ordering must therefore be examined together with the prescribed phase-locking structure.

Recent studies have also developed stability and synchronization criteria for stochastic systems with more general delay and noise structures. Zhang et al. [20] investigate semi-global synchronization of stochastic mixed time-delay systems driven by Lévy noise under aperiodic intermittent delayed sampled-data control. Zhang et al. [21] study exponential stability of highly nonlinear delayed stochastic systems with regime-switching diffusion under asynchronous intermittent control. For multi-linked stochastic delayed networks with stochastic hybrid impulses, Zhang et al. [22] derive mean-square exponential stability criteria using Dupire's functional Itô formula, Lyapunov methods, and graph theory. These contributions establish a broader context for stability analysis under combined delays and stochastic perturbations. The present study focuses on an uncontrolled four-oscillator ring with Wiener multiplicative noise and examines the ordering of amplitude-density transitions and local zero-state sample-stability changes within a delay-selected rotating-wave window. This distinction connects the stability literature to the CPG question of whether a nonzero rhythmic output persists as noise increases.

A further difficulty arises from the infinite-dimensional history space of the stochastic delay differential equation. Unified calculations of critical spectra, center dynamics, periodic branches, Floquet multipliers, stationary probability densities, and stochastic Lyapunov exponents are then computationally cumbersome. Galerkin–Koornwinder approximations convert delay equations into finite-dimensional systems while retaining the current endpoint through a point-mass inner product [23]. Subsequent developments have demonstrated their ability to preserve bifurcation structures and to construct effective reduced models for deterministic and stochastic delay systems [24, 25]. Nevertheless, the connection among SGK truncation, the delay-selected quadrupedal phase mode, the complete deterministic periodic window, and the relative locations of the stochastic P- and D-bifurcation boundaries has received limited attention within a unified framework.

Motivated by this gap, the present study considers a four-oscillator Stuart–Landau CPG with delayed unidirectional coupling and Itô-type multiplicative noise. The original deterministic DDE is used to identify the delay-selected critical spatial mode, establish its adjacent phase shift of $\pi/2$, and validate the rotating-wave structure. The SGK approximation then provides finite-dimensional deterministic and stochastic systems. The $N = 8$ system is used as the principal computational compromise, while $N = 9$ and $N = 10$ provide representative truncation checks; it is not claimed that every stochastic boundary has been fully converged with respect to order. An auxiliary direct center-projection model supplies local indicators for the P- and D-transition mechanisms. Sampled-grid P brackets and zero-state D estimates are computed for the full $N = 8$ SGK stochastic system, and an additional multi-seed audit is used to quantify the protocol sensitivity of the D estimate at $\tau = 2.50$. Periodic continuation and Floquet analysis show that the quarter-cycle rotating-wave branch occupies a bounded delay interval enclosed by two Hopf points. The corresponding conclusions for the original infinite-dimensional stochastic delay equation are interpreted only as finite-order SGK numerical evidence.

The remainder of the paper is organized as follows. Section 2 formulates the stochastic delayed CPG and its SGK approximation. Section 3 develops the deterministic and stochastic bifurcation analysis. Section 4 introduces the delay-selection criteria. Section 5 presents the numerical validation and the associated dynamical mechanisms. Section 6 concludes the paper.

The contribution is computational and methodological: Existing SGK, Hopf, and stochastic-bifurcation tools are combined for this delayed oscillator network. No new Hopf theory or SGK convergence theorem is claimed. The finite-order stochastic boundaries remain numerical estimates, and selected higher-order checks do not establish convergence to the original SDDE.

2. Stochastic time-delayed CPG model and SGK reduction

2.1. Stuart-Landau oscillator and stochastic time-delayed CPG network

After neglecting the nonlinear frequency-shift term, a single Stuart-Landau oscillator is written as

$$\dot{z}(t) = (\alpha + \mathrm{i}\omega_0)z(t) - |z(t)|^2 z(t), \qquad z(t) \in \mathbb{C}, \tag{1}$$

where α is the linear growth rate, ω_0 is the natural angular frequency, and $-|z|^2 z$ is the cubic saturation term. For $\alpha > 0$, Eq (1) possesses a stable limit cycle of amplitude $\sqrt{\alpha}$. Neglecting the nonlinear frequency shift decouples the oscillation frequency from the amplitude and therefore facilitates the use of phase differences as gait variables.

To represent stochastic fluctuations in the oscillator growth rate, Itô-type multiplicative white noise is introduced into the jth oscillator. The unidirectionally coupled four-oscillator ring network is defined by

$$\begin{aligned} \mathrm{d}z_j(t) = \Big[&(\alpha + \mathrm{i}\omega_0)z_j(t) - |z_j(t)|^2 z_j(t) \\ &+ K_c\big(z_{j-1}(t-\tau) - z_j(t)\big)\Big]\mathrm{d}t + \sigma z_j(t)\,\mathrm{d}W_j(t), \qquad j = 1, 2, 3, 4, \end{aligned} \tag{2}$$

with the cyclic convention $z_0 = z_4$. Here, $K_c \geq 0$ denotes the coupling strength, $\tau > 0$ is the transmission delay, $\sigma \geq 0$ is the noise intensity, and $W_1, \ldots, W_4$ are mutually independent standard real-valued Wiener processes. Each oscillator is associated with only one real Wiener process, and the same stochastic increment acts simultaneously on the real and imaginary parts of its complex state. This noise term can be interpreted as a random fluctuation in the linear growth rate. The Itô interpretation is used throughout this study.

Because the multiplicative diffusion coefficient vanishes at $z_j = 0$, the instantaneous term, delayed term, and diffusion term all vanish whenever the entire history segment is identically zero. Consequently, the zero history generates an absorbing equilibrium of the stochastic system. Physically, this zero state represents vanishing oscillation amplitudes and hence the loss of rhythmic CPG output. Convergence toward it corresponds to the decay of all four oscillator amplitudes to zero; once the entire history is zero, the model cannot restart the rhythm without an external perturbation. This boundary property directly affects the stationary amplitude density and the subsequent local P- and D-transition indicators.

2.2. Target quarter-cycle phase pattern and study parameters

A CPG-level rotating-wave pattern commonly associated with quadrupedal walking requires successive oscillators to be separated by one quarter of a cycle. The target phase vector is chosen as

$\boldsymbol{\phi}^d = \begin{bmatrix} 0 & \pi/2 & \pi & 3\pi/2 \end{bmatrix}^{\mathsf{T}}$. For a nonzero complex state, let $\phi_j(t) = \arg z_j(t)$. The ideal quarter-cycle relationship is

$$\phi_{j+1}(t) - \phi_j(t) \equiv \frac{\pi}{2} \pmod{2\pi}, \qquad j = 1, 2, 3, \tag{3}$$

and the ring closure condition gives $\phi_1 - \phi_4 \equiv \pi/2 \pmod{2\pi}$. In this paper, this phase pattern is interpreted as a CPG-level quarter-cycle rotating wave relevant to quadrupedal walking. No unique oscillator-to-leg assignment, duty-factor law, body dynamics, or foot–ground contact model is imposed; consequently, the calculations do not by themselves validate a physical robot gait. To remove the invariance associated with a uniform phase shift, the relative phase error is defined as

$$E_\phi(t) = \left\{ \frac{1}{4} \sum_{j=1}^{4} \left[\mathrm{wrap}_{[-\pi,\pi)} \Big([\phi_j(t) - \phi_1(t)] - [\phi_j^d - \phi_1^d] \Big) \right]^2 \right\}^{1/2}. \tag{4}$$

The delay τ is used as the primary tuning parameter, whereas the noise intensity σ is treated as the stochastic bifurcation parameter. The remaining parameters determine the intrinsic frequency, local growth rate, and coupling strength. In the following analysis, the original infinite-dimensional stochastic delay equation is first approximated by a finite-dimensional stochastic system using the stochastic Galerkin–Koornwinder approximation (SGK). The Hopf bifurcation of the quarter-cycle mode, the auxiliary direct-projection transition indicators, and the full $N = 8$ SGK stochastic operating region are then investigated.

2.3. Complex vector form and eight-dimensional real-state representation

Introduce the complex state vector and the cyclic predecessor operator as

$$\boldsymbol{z}(t) = \begin{bmatrix} z_1(t) & z_2(t) & z_3(t) & z_4(t) \end{bmatrix}^{\mathsf{T}} \in \mathbb{C}^4, \qquad \boldsymbol{P}\boldsymbol{z} = \mathrm{col}(z_4, z_1, z_2, z_3).$$

Thus, under the cyclic convention, the jth component of $\boldsymbol{P}\boldsymbol{z}(t-\tau)$ is $z_{j-1}(t-\tau)$. For compact notation, define

$$\boldsymbol{L}_c = (\alpha - K_c + \mathrm{i}\omega_0)\boldsymbol{I}_4, \qquad \boldsymbol{M}_c = K_c \boldsymbol{P},$$
$$\boldsymbol{N}_c(\boldsymbol{z}) = -\mathrm{col}\Big(|z_1|^2 z_1, \ldots, |z_4|^2 z_4 \Big).$$

Equation (2) can then be written in the compact form

$$\mathrm{d}\boldsymbol{z}(t) = [\boldsymbol{L}_c \boldsymbol{z}(t) + \boldsymbol{M}_c \boldsymbol{z}(t-\tau) + \boldsymbol{N}_c(\boldsymbol{z}(t))]\mathrm{d}t + \sigma\, \mathrm{diag}(\boldsymbol{z}(t))\, \mathrm{d}\boldsymbol{W}(t), \tag{5}$$

where $\boldsymbol{W} = (W_1, W_2, W_3, W_4)^{\mathsf{T}}$. The delay appears only in the cyclic predecessor-coupling term, whereas the multiplicative noise acts directly on the local complex state of each oscillator.

Writing each complex oscillator in real coordinates, set

$$z_j = x_j + \mathrm{i}y_j, \qquad \boldsymbol{X}_j = \begin{bmatrix} x_j & y_j \end{bmatrix}^{\mathsf{T}}, \qquad \boldsymbol{X} = \mathrm{col}(\boldsymbol{X}_1, \boldsymbol{X}_2, \boldsymbol{X}_3, \boldsymbol{X}_4) \in \mathbb{R}^8.$$

The corresponding linear real-state matrices are

$$\boldsymbol{A}_s = \begin{bmatrix} \alpha - K_c & -\omega_0 \\ \omega_0 & \alpha - K_c \end{bmatrix}, \qquad \boldsymbol{A}_0 = \boldsymbol{I}_4 \otimes \boldsymbol{A}_s, \qquad \boldsymbol{B}_0 = K_c \boldsymbol{P} \otimes \boldsymbol{I}_2.$$

The cubic nonlinearity is written blockwise as

$$\boldsymbol{F}(\boldsymbol{X}) = \mathrm{col}(\boldsymbol{f}_1, \ldots, \boldsymbol{f}_4), \qquad \boldsymbol{f}_j = -r_j^2 \boldsymbol{X}_j, \qquad r_j^2 = x_j^2 + y_j^2.$$

For $j = 1, \ldots, 4$, let $\boldsymbol{E}_j \in \mathbb{R}^{8\times 8}$ denote the coordinate-selection matrix of the jth oscillator; that is, only the $(2j-1)$-th and $2j$-th diagonal entries of $\boldsymbol{E}_j$ are equal to one. The physical diffusion matrix is

$$\boldsymbol{G}(\boldsymbol{X}) = \begin{bmatrix} \boldsymbol{E}_1\boldsymbol{X} & \boldsymbol{E}_2\boldsymbol{X} & \boldsymbol{E}_3\boldsymbol{X} & \boldsymbol{E}_4\boldsymbol{X} \end{bmatrix} \in \mathbb{R}^{8\times 4}.$$

Accordingly, the original infinite-dimensional stochastic delay equation is equivalent to

$$\mathrm{d}\boldsymbol{X}(t) = [\boldsymbol{A}_0\boldsymbol{X}(t) + \boldsymbol{B}_0\boldsymbol{X}(t-\tau) + \boldsymbol{F}(\boldsymbol{X}(t))]\mathrm{d}t + \sigma\boldsymbol{G}(\boldsymbol{X}(t))\,\mathrm{d}\boldsymbol{W}(t). \tag{6}$$

The diffusion matrix satisfies

$$\boldsymbol{G}(\boldsymbol{0}) = \boldsymbol{0}, \qquad \boldsymbol{G}(c\boldsymbol{X}) = c\boldsymbol{G}(\boldsymbol{X}), \tag{7}$$

and

$$\boldsymbol{G}(\boldsymbol{X})\boldsymbol{G}(\boldsymbol{X})^{\mathsf{T}} = \mathrm{blockdiag}\Big(\boldsymbol{X}_1\boldsymbol{X}_1^{\mathsf{T}}, \boldsymbol{X}_2\boldsymbol{X}_2^{\mathsf{T}}, \boldsymbol{X}_3\boldsymbol{X}_3^{\mathsf{T}}, \boldsymbol{X}_4\boldsymbol{X}_4^{\mathsf{T}}\Big). \tag{8}$$

Hence, $\boldsymbol{G}(\boldsymbol{X})$ is not an eight-dimensional diagonal diffusion matrix. The system contains four independent real Wiener processes rather than one independent noise source for each of the eight real state components.

Given an initial history function $\boldsymbol{\varphi} \in C([-\tau, 0], \mathbb{R}^8)$, the system satisfies $\boldsymbol{X}(t) = \boldsymbol{\varphi}(t)$ for $t \in [-\tau, 0]$. The deterministic drift consists of the linear delayed term and a dissipative cubic term, for which

$$\langle \boldsymbol{X}, \boldsymbol{F}(\boldsymbol{X})\rangle = -\sum_{j=1}^{4}(x_j^2 + y_j^2)^2 \le 0. \tag{9}$$

Thus, the cubic term provides dissipation at large amplitudes.

2.4. History space and Koornwinder basis

Define the history segment by $\boldsymbol{X}_t(\theta) = \boldsymbol{X}(t+\theta)$ for $\theta \in [-\tau, 0]$, and introduce the linear transformation $s = 1 + 2\theta/\tau$, equivalently $\theta = \tau(s-1)/2$, with $s \in [-1, 1]$. Thus, the current endpoint $\theta = 0$ corresponds to $s = 1$, whereas the delayed endpoint $\theta = -\tau$ corresponds to $s = -1$.

The Koornwinder basis is first constructed in the scalar Hilbert space $\mathcal{E} = L^2([-1, 1]) \times \mathbb{R}$ and is then applied componentwise to $\mathbb{R}^8$-valued history segments. The space $\mathcal{E}$ is equipped with the endpoint-mass inner product

$$\langle f, g\rangle_{\mathcal{E}} = \frac{1}{2}\int_{-1}^{1} f(s)g(s)\,\mathrm{d}s + f(1)g(1). \tag{10}$$

Let $K_p(s)$ denote the Koornwinder polynomials orthogonal with respect to the inner product (10), normalized by $K_p(1) = 1$. Their left-endpoint values and squared norms are

$$\kappa_p := K_p(-1) = (-1)^p(p^2 + p + 1), \qquad q_p := \|K_p\|_{\mathcal{E}}^2 = \frac{(p^2+1)((p+1)^2+1)}{2p+1}.$$

Because the degree of K_p' does not exceed $p-1$, there exists a unique set of coefficients a_{pk} such that $\mathrm{d}K_p(s)/\mathrm{d}s = \sum_{k=0}^{p-1} a_{pk}K_k(s)$ for $p \ge 1$.

2.5. Truncated expansion and endpoint reconstruction

Using the first N basis functions, the history segment is approximated by the truncated expansion

$$\boldsymbol{X}_t(\theta) \approx \boldsymbol{X}_t^{(N)}(\theta) = \sum_{p=0}^{N-1} \boldsymbol{y}_p(t) K_p\left(1 + \frac{2\theta}{\tau}\right), \qquad \boldsymbol{y}_p(t) \in \mathbb{R}^8. \tag{11}$$

By $K_p(1) = 1$ and the definition of κ_p, the current and delayed states are reconstructed as

$$\boldsymbol{X}_c(t) = \boldsymbol{X}_t^{(N)}(0) = \sum_{p=0}^{N-1} \boldsymbol{y}_p(t). \tag{12}$$

$$\boldsymbol{X}_{c\tau}(t) = \boldsymbol{X}_t^{(N)}(-\tau) = \sum_{p=0}^{N-1} \kappa_p \boldsymbol{y}_p(t). \tag{13}$$

Collect the modal coefficients in the global vector

$$\boldsymbol{Y}(t) = \mathrm{col}\big(\boldsymbol{y}_0(t), \boldsymbol{y}_1(t), \ldots, \boldsymbol{y}_{N-1}(t)\big) \in \mathbb{R}^{8N},$$

and define the current- and delayed-endpoint reconstruction matrices by

$$\boldsymbol{C}_0 = \begin{bmatrix} \boldsymbol{I}_8 & \boldsymbol{I}_8 & \cdots & \boldsymbol{I}_8 \end{bmatrix}, \qquad \boldsymbol{C}_\tau = \begin{bmatrix} \kappa_0 \boldsymbol{I}_8 & \kappa_1 \boldsymbol{I}_8 & \cdots & \kappa_{N-1} \boldsymbol{I}_8 \end{bmatrix}.$$

Then $\boldsymbol{X}_c = \boldsymbol{C}_0 \boldsymbol{Y}$ and $\boldsymbol{X}_{c\tau} = \boldsymbol{C}_\tau \boldsymbol{Y}$.

2.6. Galerkin-Koornwinder projection

The history translation satisfies $\partial_t \boldsymbol{X}_t = \partial_\theta \boldsymbol{X}_t$. Together with this mapping, this gives $\partial_\theta = (2/\tau)\partial_s$. Substituting expansion (11) into the history-translation equation and using the Koornwinder orthogonality relations yields the projected transport coefficients

$$T_{\ell p}(\tau) = \frac{2}{\tau q_\ell} \sum_{k=0}^{p-1} a_{pk}(q_\ell \delta_{\ell k} - 1), \qquad \ell, p = 0, \ldots, N-1, \tag{14}$$

where the empty sum is taken as zero for $p = 0$. At the current endpoint, the physical vector field is injected into the ℓth mode with the factor $K_\ell(1)/q_\ell = 1/q_\ell$. Therefore, the ℓth SGK coefficient satisfies

$$\begin{aligned} \mathrm{d}\boldsymbol{y}_\ell = & \left\{ \sum_{p=0}^{N-1} T_{\ell p}(\tau) \boldsymbol{y}_p + \frac{1}{q_\ell} \big[\boldsymbol{A}_0 \boldsymbol{X}_c + \boldsymbol{B}_0 \boldsymbol{X}_{c\tau} + \boldsymbol{F}(\boldsymbol{X}_c) \big] \right\} \mathrm{d}t \\ & + \frac{\sigma}{q_\ell} \boldsymbol{G}(\boldsymbol{X}_c)\, \mathrm{d}\boldsymbol{W}(t), \qquad \ell = 0, \ldots, N-1. \end{aligned} \tag{15}$$

Equation (15) contains no explicit delay. The delay information is retained through $T_{\ell p}(\tau)$ and the left-endpoint reconstruction $\boldsymbol{X}_{c\tau}$.

2.7. Finite-dimensional stochastic system and structural properties

Define the (ℓ, p) block of $\boldsymbol{A}_{\mathrm{SGK}}(\tau) \in \mathbb{R}^{8N\times 8N}$ by

$$[\boldsymbol{A}_{\mathrm{SGK}}(\tau)]_{\ell p} = T_{\ell p}(\tau)\boldsymbol{I}_8 + \frac{1}{q_\ell}\boldsymbol{A}_0 + \frac{\kappa_p}{q_\ell}\boldsymbol{B}_0. \tag{16}$$

The nonlinear term is written as

$$\boldsymbol{\mathcal{G}}_{\mathrm{SGK}}(\boldsymbol{Y}) = \mathrm{col}\left(\frac{1}{q_0}\boldsymbol{F}(\boldsymbol{C}_0\boldsymbol{Y}), \frac{1}{q_1}\boldsymbol{F}(\boldsymbol{C}_0\boldsymbol{Y}), \ldots, \frac{1}{q_{N-1}}\boldsymbol{F}(\boldsymbol{C}_0\boldsymbol{Y})\right). \tag{17}$$

To represent the projection of the multiplicative noise, define the injection operator from the current physical state into the SGK space as

$$\boldsymbol{J}_N = \mathrm{col}\left(\frac{K_0(1)}{q_0}\boldsymbol{I}_8, \frac{K_1(1)}{q_1}\boldsymbol{I}_8, \ldots, \frac{K_{N-1}(1)}{q_{N-1}}\boldsymbol{I}_8\right) = \mathrm{col}\left(q_0^{-1}\boldsymbol{I}_8, \ldots, q_{N-1}^{-1}\boldsymbol{I}_8\right). \tag{18}$$

The SGK diffusion matrix is

$$\boldsymbol{B}_{\mathrm{SGK}}(\boldsymbol{Y}) = \boldsymbol{J}_N\boldsymbol{G}(\boldsymbol{C}_0\boldsymbol{Y}) \in \mathbb{R}^{8N\times 4}. \tag{19}$$

Define the four noise-channel operators

$$\boldsymbol{L}_j = \boldsymbol{J}_N\boldsymbol{E}_j\boldsymbol{C}_0 \in \mathbb{R}^{8N\times 8N}, \qquad j = 1, 2, 3, 4. \tag{20}$$

Thus,

$$\boldsymbol{B}_{\mathrm{SGK}}(\boldsymbol{Y}) = \begin{bmatrix}\boldsymbol{L}_1\boldsymbol{Y} & \boldsymbol{L}_2\boldsymbol{Y} & \boldsymbol{L}_3\boldsymbol{Y} & \boldsymbol{L}_4\boldsymbol{Y}\end{bmatrix}. \tag{21}$$

The resulting $8N$-dimensional Itô stochastic system, which contains no explicit delay, is

$$\mathrm{d}\boldsymbol{Y}(t) = [\boldsymbol{A}_{\mathrm{SGK}}(\tau)\boldsymbol{Y}(t) + \boldsymbol{\mathcal{G}}_{\mathrm{SGK}}(\boldsymbol{Y}(t))]\mathrm{d}t + \sigma\boldsymbol{B}_{\mathrm{SGK}}(\boldsymbol{Y}(t))\,\mathrm{d}\boldsymbol{W}(t). \tag{22}$$

Equations (7) and (19) imply

$$\boldsymbol{B}_{\mathrm{SGK}}(\boldsymbol{0}) = \boldsymbol{0}, \qquad \boldsymbol{B}_{\mathrm{SGK}}(c\boldsymbol{Y}) = c\boldsymbol{B}_{\mathrm{SGK}}(\boldsymbol{Y}). \tag{23}$$

Moreover, $\boldsymbol{\mathcal{G}}_{\mathrm{SGK}}(\boldsymbol{0}) = \boldsymbol{0}$; hence, the zero state remains an absorbing equilibrium. When $\sigma = 0$, Eq (22) reduces to the deterministic SGK system. Its Hopf critical point, periodic branch, and deterministic stability boundary are therefore unaffected by the form of the stochastic forcing. Collocation schemes provide another finite-dimensional route for stochastic delay equations [26]; the SGK construction is adopted here because its endpoint reconstruction is directly compatible with the spectral, continuation, and stochastic calculations used below. The truncation order N is selected by jointly examining convergence of the critical spectrum, time histories, phase error, and stochastic projection coefficients.

Four model levels are distinguished throughout the remainder of the paper. The term *original deterministic DDE* refers to Eq (2) with $\sigma = 0$, and is used for the direct DDE spectrum, critical frequency, rotating-wave structure, and deterministic trajectory checks. The term *original infinite-dimensional stochastic delay equation* refers to Eq (2) with $\sigma > 0$; the stochastic SGK results provide numerical evidence for this equation but are not presented as a rigorous infinite-dimensional P- or

D-bifurcation theorem. Equation (22), including all $8N$ variables, is called the *full Nth-order SGK stochastic system*; the principal computations use the full $N = 8$ SGK stochastic system. Finally, the projection derived in Section 3.3 is called the *auxiliary direct center-projection model*; it supplies local analytical transition indicators but is not identified with either the full Nth-order SGK stochastic system or the original infinite-dimensional stochastic delay equation.

3. Deterministic dynamics and auxiliary P–D transition indicators

3.1. Linear spectrum and Hopf bifurcation conditions

Sections 3.1 and 3.2 concern the deterministic Nth-order SGK system near its Hopf point. Sections 3.3 and 3.4 introduce the auxiliary direct center-projection model. The resulting analytical P- and D-thresholds are local transition indicators and are not identified with the numerical boundaries of the full Nth-order SGK stochastic system. Numerical definitions for the full Nth-order SGK stochastic system are introduced separately at the end of Section 3.4. Throughout Section 3, τ_c and Ω_c denote the Hopf delay and critical frequency of the selected deterministic Nth-order SGK system; Section 5 specializes these quantities to $N = 8$.

Let $\boldsymbol{\mathcal{F}}(\boldsymbol{Y}, \tau) = \boldsymbol{A}_{\mathrm{SGK}}(\tau)\boldsymbol{Y} + \boldsymbol{\mathcal{G}}_{\mathrm{SGK}}(\boldsymbol{Y})$. Because $\boldsymbol{\mathcal{G}}_{\mathrm{SGK}}(\boldsymbol{0}) = \boldsymbol{0}$ and $D\boldsymbol{\mathcal{G}}_{\mathrm{SGK}}(\boldsymbol{0}) = \boldsymbol{0}$, the deterministic system $\dot{\boldsymbol{Y}} = \boldsymbol{\mathcal{F}}(\boldsymbol{Y}, \tau)$ has the linearization $\dot{\boldsymbol{Y}} = \boldsymbol{A}_{\mathrm{SGK}}(\tau)\boldsymbol{Y}$ at the origin.

The finite-dimensional characteristic equation is defined by

$$\Delta_N(\lambda, \tau) := \det(\lambda \boldsymbol{I}_{8N} - \boldsymbol{A}_{\mathrm{SGK}}(\tau)) = 0. \tag{24}$$

Assume that there exist a critical delay τ_c and a critical frequency $\Omega_c > 0$ such that

$$\lambda_{1,2}(\tau_c) = \pm \mathrm{i}\Omega_c, \qquad \text{with a simple critical eigenvalue pair.} \tag{25}$$

$$\mathrm{Re}\, \lambda_j(\tau_c) < 0, \qquad j = 3, \ldots, 8N. \tag{26}$$

$$\frac{\mathrm{d}}{\mathrm{d}\tau} \mathrm{Re}\, \lambda_1(\tau)\Big|_{\tau=\tau_c} \neq 0. \tag{27}$$

Conditions (25)–(26) ensure that the critical center subspace is two-dimensional, whereas Eq (27) is the transversality condition.

Let $\boldsymbol{A}_c = \boldsymbol{A}_{\mathrm{SGK}}(\tau_c)$, and choose the right and left critical eigenvectors $\boldsymbol{v}, \boldsymbol{u} \in \mathbb{C}^{8N}$ such that

$$\boldsymbol{A}_c \boldsymbol{v} = \mathrm{i}\Omega_c \boldsymbol{v}, \qquad \boldsymbol{A}_c^* \boldsymbol{u} = -\mathrm{i}\Omega_c \boldsymbol{u}, \qquad \boldsymbol{u}^* \boldsymbol{v} = 1. \tag{28}$$

Differentiating $\boldsymbol{A}_{\mathrm{SGK}}(\tau)\boldsymbol{v}(\tau) = \lambda(\tau)\boldsymbol{v}(\tau)$ with respect to τ and premultiplying by $\boldsymbol{u}^*$ yields $\lambda'(\tau_c) = \boldsymbol{u}^* \boldsymbol{A}_\tau \boldsymbol{v}$, where $\boldsymbol{A}_\tau := \partial \boldsymbol{A}_{\mathrm{SGK}}/\partial\tau|_{\tau=\tau_c}$. According to Eq (14), only the transport term of $\boldsymbol{A}_{\mathrm{SGK}}$ depends explicitly on τ, so that $[\boldsymbol{A}_\tau]_{\ell p} = -T_{\ell p}(\tau_c)\boldsymbol{I}_8/\tau_c$. Define the transversality coefficient as $\chi = \mathrm{Re}(\boldsymbol{u}^* \boldsymbol{A}_\tau \boldsymbol{v})$.

If $\chi \neq 0$, the critical conjugate pair crosses the imaginary axis transversely as τ varies. Therefore, if Eqs (25)–(27) hold, the deterministic SGK system satisfies the spectral conditions for a Hopf bifurcation near $\tau = \tau_c$.

3.2. Center manifold, normal form, and critical quarter-cycle mode

Let $\eta = \tau - \tau_c$. Since $\mathcal{G}_{\mathrm{SGK}}$ is a homogeneous cubic nonlinearity, the vector field near $(\boldsymbol{Y}, \eta) = (\boldsymbol{0}, 0)$ can be expanded as

$$\mathcal{F}(\boldsymbol{Y}, \tau_c + \eta) = \boldsymbol{A}_c \boldsymbol{Y} + \eta \boldsymbol{A}_\tau \boldsymbol{Y} + \frac{1}{6}\boldsymbol{C}(\boldsymbol{Y}, \boldsymbol{Y}, \boldsymbol{Y}) + O\Big(\eta^2\|\boldsymbol{Y}\| + |\eta|\|\boldsymbol{Y}\|^3 + \|\boldsymbol{Y}\|^5\Big), \tag{29}$$

where $\boldsymbol{C} : (\mathbb{C}^{8N})^3 \to \mathbb{C}^{8N}$ is the symmetric trilinear operator determined by the third-order derivative. The critical center subspace is $E_c = \mathrm{span}\{\boldsymbol{v}, \bar{\boldsymbol{v}}\}$. Define the spectral projections by $\boldsymbol{P}_c = \boldsymbol{v}\boldsymbol{u}^* + \bar{\boldsymbol{v}}\,\bar{\boldsymbol{u}}^*$ and $\boldsymbol{P}_s = \boldsymbol{I} - \boldsymbol{P}_c$.

The local center manifold can be represented as

$$\boldsymbol{Y} = w\boldsymbol{v} + \bar{w}\,\bar{\boldsymbol{v}} + \boldsymbol{h}(w, \bar{w}, \eta), \qquad \boldsymbol{P}_c\boldsymbol{h} = \boldsymbol{0}, \tag{30}$$

where $\boldsymbol{h}(w, \bar{w}, \eta) = O(|w|^3 + |\eta||w|)$.

Because the system contains no quadratic nonlinearity, all second-order center-manifold coefficients vanish. Center-manifold and normal-form reductions provide a standard route for resolving Hopf dynamics in delayed systems [11]. The nonresonant cubic terms are uniquely determined by the corresponding homological equations, whereas the resonant term $w^2\bar{w}$ remains in the center normal form.

Using the center coordinate $w = \boldsymbol{u}^*\boldsymbol{Y}$, substituting Eq (30) into Eq (29), and projecting onto E_c gives

$$\dot{w} = (\mathrm{i}\Omega_c + \nu\eta)w + c_H w|w|^2 + O\Big(|w|^5 + |\eta||w|^3 + \eta^2|w|\Big), \tag{31}$$

where $\nu = \boldsymbol{u}^*\boldsymbol{A}_\tau\boldsymbol{v}$ and $c_H = \boldsymbol{u}^*\boldsymbol{C}(\boldsymbol{v}, \boldsymbol{v}, \bar{\boldsymbol{v}})/2$. The factor 1/2 arises from the three permutations of $w^2\bar{w}$ in the trilinear term. Let $\beta = \mathrm{Re}(\nu)\eta = \chi(\tau - \tau_c)$, $\Omega(\tau) = \Omega_c + \mathrm{Im}(\nu)\eta$, and $c_H = a + \mathrm{i}b$. Writing $w = r\exp(\mathrm{i}\theta)$, Eq (31) becomes

$$\begin{aligned} \dot{r} &= \beta r + ar^3 + O\Big(r^5 + |\eta|r^3 + \eta^2 r\Big), \\ \dot{\theta} &= \Omega(\tau) + br^2 + O\Big(r^4 + |\eta|r^2\Big). \end{aligned} \tag{32}$$

If $\chi > 0$ and $a < 0$, a supercritical Hopf bifurcation occurs as τ increases through τ_c. For $\tau > \tau_c$ and sufficiently small β, a stable small-amplitude periodic solution exists, whose center amplitude satisfies

$$r_*(\tau) = \sqrt{-\frac{\beta}{a}} + O\Big(|\beta|^{3/2}\Big). \tag{33}$$

The current physical state is reconstructed from $\boldsymbol{X}_c = \boldsymbol{C}_0\boldsymbol{Y}$. Let $\boldsymbol{U} = \boldsymbol{C}_0\boldsymbol{v} \in \mathbb{C}^8$ and $\zeta_j = U_{2j-1} + \mathrm{i}U_{2j}$ for $j = 1, 2, 3, 4$.

The positive-rotation fundamental harmonic of the jth oscillator along the critical eigendirection is defined as

$$\widehat{z}_j^{(1)}(t) = w(t)\zeta_j = r(t)\rho_j \exp\Big(\mathrm{i}[\theta(t) + \phi_j^0]\Big), \qquad \rho_j = |\zeta_j|, \quad \phi_j^0 = \arg\zeta_j. \tag{34}$$

The critical eigenvector is selected to correspond to the positive-rotation branch of the original complex system. Under this choice, Eq (34) gives the linear fundamental harmonic of the physical complex state, while the higher-order center-manifold terms are asymptotically smaller. Therefore, in

the Hopf critical limit, the relative phases are determined by the arguments of ζ_j. If there exists a global phase ϕ_0 such that $\phi_j^0 \equiv \phi_j^d + \phi_0 \pmod{2\pi}$ for $j = 1, 2, 3, 4$, then the critical Hopf mode has a $\pi/2$ phase shift between neighboring oscillators and therefore generates the target quarter-cycle rotating-wave branch.

3.3. Auxiliary direct center-projection model, amplitude equation, and stationary density under multiplicative noise

According to Eq (21), the four noise channels of the stochastic SGK system are linear state operators. Taking $w = \boldsymbol{u}^* \boldsymbol{Y}$ as the center coordinate and substituting Eq (30) into the stochastic system, while retaining the deterministic cubic term and the terms that are linear in $(w, \bar{w})$ in the diffusion, gives the auxiliary direct center-projection model

$$\begin{aligned} \mathrm{d}w = &\Big[(\beta + \mathrm{i}\Omega(\tau))w + c_H w|w|^2 + R_d(w, \bar{w}, \eta)\Big]\mathrm{d}t \\ &+ \sigma \sum_{j=1}^{4} \Big[\gamma_j w + \delta_j \bar{w} + R_j(w, \bar{w}, \eta)\Big]\mathrm{d}W_j(t), \end{aligned} \tag{35}$$

where $\gamma_j = \boldsymbol{u}^* \boldsymbol{L}_j \boldsymbol{v}$ and $\delta_j = \boldsymbol{u}^* \boldsymbol{L}_j \bar{\boldsymbol{v}}$, and

$$R_d = O\Big(|w|^5 + |\eta||w|^3 + \eta^2|w|\Big), \qquad R_j = O\Big(|w|^2 + |\eta||w|\Big). \tag{36}$$

The linear projection $w = \boldsymbol{u}^* \boldsymbol{Y}$ itself does not generate an Itô correction. The Itô terms appearing below arise from the nonlinear transformation from the complex center coordinate to polar coordinates. Equation (35) defines the auxiliary direct center-projection model based on the deterministic center manifold. If a noise channel couples the center mode to the stable complement, the corresponding feedback is contained in the higher-order stochastic corrections.

Let $\boldsymbol{J}_2 = \left[\begin{smallmatrix} 0 & -1 \\ 1 & 0 \end{smallmatrix}\right]$, $\boldsymbol{J}_8 = \boldsymbol{I}_4 \otimes \boldsymbol{J}_2$, and $\mathcal{J}_N = \boldsymbol{I}_N \otimes \boldsymbol{J}_8$.

The blockwise complex-linear structure of $\boldsymbol{A}_0$, $\boldsymbol{B}_0$, and $\boldsymbol{E}_j$ implies

$$\boldsymbol{A}_{\mathrm{SGK}} \mathcal{J}_N = \mathcal{J}_N \boldsymbol{A}_{\mathrm{SGK}}, \qquad \boldsymbol{L}_j \mathcal{J}_N = \mathcal{J}_N \boldsymbol{L}_j. \tag{37}$$

For a simple critical eigenvalue, the right and left eigenvectors can be chosen with positive-rotation polarization such that $\mathcal{J}_N \boldsymbol{v} = \mathrm{i}\boldsymbol{v}$ and $\mathcal{J}_N \boldsymbol{u} = \mathrm{i}\boldsymbol{u}$. Consequently, $\boldsymbol{L}_j \bar{\boldsymbol{v}}$ lies in the $-\mathrm{i}$ eigenspace of $\mathcal{J}_N$ and is orthogonal to $\boldsymbol{u}$, giving

$$\delta_j = \boldsymbol{u}^* \boldsymbol{L}_j \bar{\boldsymbol{v}} = 0, \qquad j = 1, 2, 3, 4. \tag{38}$$

Thus, $\delta_j = 0$ follows from the complex-linear structure and is not a numerical round-off assumption. Neglecting the higher-order terms in Eq (36) yields the truncated center model used for the local stochastic bifurcation analysis:

$$\mathrm{d}w = \Big[(\beta + \mathrm{i}\Omega(\tau))w + c_H w|w|^2\Big]\mathrm{d}t + \sigma w \sum_{j=1}^{4} \gamma_j \, \mathrm{d}W_j(t). \tag{39}$$

Let $w = r\exp(\mathrm{i}\theta)$ and define

$$\begin{aligned} q_r &= \sum_{j=1}^{4}(\operatorname{Re}\gamma_j)^2, \quad q_\theta = \sum_{j=1}^{4}(\operatorname{Im}\gamma_j)^2, \\ \kappa_r &= \frac{1}{2}q_\theta, \qquad\qquad \kappa_\theta = -\sum_{j=1}^{4}\operatorname{Re}\gamma_j \operatorname{Im}\gamma_j. \end{aligned} \tag{40}$$

Applying Itô's formula to $r = |w|$ and $\theta = \arg w$ gives

$$\mathrm{d}r = \Big[(\beta + \sigma^2\kappa_r)r + ar^3\Big]\mathrm{d}t + \sigma r\sum_{j=1}^{4}\operatorname{Re}\gamma_j\,\mathrm{d}W_j(t), \qquad r > 0. \tag{41}$$

$$\mathrm{d}\theta = \Big[\Omega(\tau) + br^2 + \sigma^2\kappa_\theta\Big]\mathrm{d}t + \sigma\sum_{j=1}^{4}\operatorname{Im}\gamma_j\,\mathrm{d}W_j(t). \tag{42}$$

For $q_r > 0$, define $B_r(t) = q_r^{-1/2}\sum_{j=1}^{4}\operatorname{Re}\gamma_j\,W_j(t)$. Then B_r is a standard real-valued Wiener process, and the radial equation becomes

$$\mathrm{d}r = [\lambda_\sigma(\tau,\sigma)r + ar^3]\mathrm{d}t + \sigma\sqrt{q_r}\,r\,\mathrm{d}B_r(t), \qquad \lambda_\sigma = \beta + \sigma^2\kappa_r. \tag{43}$$

Both the drift and diffusion coefficients vanish at $r = 0$; hence, $r = 0$ is an absorbing boundary.

For a unified representation of Eq (43), set $\mu_1 = \lambda_\sigma$, $\mu_2 = a$, and $\mu_3 = \sigma^2 q_r$. The radial equation can then be written as

$$\mathrm{d}r = (\mu_1 r + \mu_2 r^3)\mathrm{d}t + \sqrt{\mu_3}\,r\,\mathrm{d}B_r(t), \qquad \mu_2 < 0. \tag{44}$$

For $\sigma > 0$, the forward Kolmogorov (Fokker–Planck–Kolmogorov) equation associated with Eq (44) on $r > 0$ is

$$\frac{\partial p}{\partial t} = -\frac{\partial}{\partial r}\Big[(\mu_1 r + \mu_2 r^3)p\Big] + \frac{\mu_3}{2}\frac{\partial^2}{\partial r^2}(r^2 p). \tag{45}$$

Under the zero-probability-flux condition, the continuous stationary density on the positive half-line is

$$p_s(r) = C_r r^m \exp\left(\frac{\mu_2}{\mu_3}r^2\right), \qquad m = \frac{2\mu_1}{\mu_3} - 2. \tag{46}$$

When $\mu_2 < 0$ and $m > -1$, this density is normalizable, with the normalization constant

$$C_r = \frac{2(-\mu_2/\mu_3)^{(m+1)/2}}{\Gamma((m+1)/2)}. \tag{47}$$

The condition $m > -1$ is equivalent to $\mu_1 > \mu_3/2$. Equations (44) and (46) provide a common local model for the D- and P-type transition criteria, respectively.

3.4. Local P–D transition indicators and full Nth-order SGK numerical definitions

Within the auxiliary direct center-projection model, the local D-type indicator is a change in the sample stability of the zero random equilibrium, whereas the local P-type indicator is a change in the extremum structure of the stationary probability density. Both criteria are based on Eq (44), but they concern different statistical objects.

3.4.1. Local D-type transition indicator

Changes in the sign of a maximal Lyapunov exponent are commonly used to identify noise-induced stability transitions in stochastic nonlinear systems [13]. Near the zero state, the linearization of Eq (44) is

$$\mathrm{d}r = \mu_1 r\,\mathrm{d}t + \sqrt{\mu_3}\, r\,\mathrm{d}B_r(t). \tag{48}$$

For $r > 0$, applying Itô's formula to $\ln r$ yields

$$\mathrm{d}\ln r = \left(\mu_1 - \frac{\mu_3}{2}\right)\mathrm{d}t + \sqrt{\mu_3}\,\mathrm{d}B_r(t). \tag{49}$$

Since $B_r(t)/t \to 0$ almost surely, the maximal Lyapunov exponent of the auxiliary direct center-projection model at the zero state is

$$\Lambda_{\mathrm{proj}}(\tau,\sigma) = \mu_1 - \frac{\mu_3}{2} = \beta(\tau) - d_r\sigma^2, \qquad d_r := \frac{q_r}{2} - \kappa_r. \tag{50}$$

When $d_r > 0$, Λ_{proj} decreases strictly with σ^2, and the D-type transition condition is $2\mu_1/\mu_3 = 1$. For $\chi > 0$, $\tau > \tau_c$, and $d_r > 0$, the truncated auxiliary projection model gives

$$\sigma_{D,\mathrm{proj}}(\tau) = \left[\frac{\chi(\tau-\tau_c)}{q_r/2 - \kappa_r}\right]^{1/2}. \tag{51}$$

Equation (51) is the threshold of the truncated auxiliary projection model. The omitted stochastic center–stable coupling and higher-order terms are not controlled here strongly enough to justify an asymptotic expansion for the boundary of an untruncated stochastic center-manifold system. Accordingly, Eq (51) is used only as a local projected indicator and as a trend predictor for the numerical full-SGK calculation.

The Lyapunov exponent Λ_{proj} is positive on one side of this boundary and negative on the other. Hence, the boundary represents a change in the sample-wise exponential stability of the zero random equilibrium, rather than a second creation or destruction of the deterministic periodic branch.

3.4.2. Local P-type transition indicator

Stationary-density extrema and most-probable-response criteria are widely used to identify stochastic P-bifurcations in nonlinear systems [27, 28]. Differentiating Eq (46) gives

$$\frac{\mathrm{d}p_s}{\mathrm{d}r} = p_s(r)\left(\frac{m}{r} + \frac{2\mu_2}{\mu_3}r\right). \tag{52}$$

An interior extremum on the positive half-line satisfies

$$r_{\mathrm{mp}}^2 = -\frac{m\mu_3}{2\mu_2}. \tag{53}$$

Because $\mu_2 < 0$, Eq (53) yields a unique positive critical point when $m > 0$. Moreover,

$$\left.\frac{p_s''(r)}{p_s(r)}\right|_{r=r_{\mathrm{mp}}} = \frac{4\mu_2}{\mu_3} < 0. \tag{54}$$

Thus, the critical point is an interior maximum. At $m = 0$, this interior maximum collapses to the boundary $r = 0$. For $-1 < m < 0$, there is no longer an interior extremum on the positive half-line, and the stationary density decreases monotonically away from the zero-amplitude boundary.

Under the extremum-structure criterion adopted here, the P-type transition condition is $m = 0$, equivalently $\mu_1/\mu_3 = 1$. Substituting $\mu_1 = \beta + \sigma^2\kappa_r$ and $\mu_3 = \sigma^2 q_r$, and noting that $d_r > 0$ implies $q_r - \kappa_r = q_r/2 + d_r > 0$, the truncated center model gives, for $\chi > 0$ and $\tau > \tau_c$,

$$\sigma_{P,\mathrm{proj}}(\tau) = \left[\frac{\chi(\tau - \tau_c)}{q_r - \kappa_r}\right]^{1/2}. \tag{55}$$

Equation (55) is likewise interpreted as the P-type threshold of the truncated auxiliary projection model. No claim is made that it is the asymptotic boundary of the full SGK stochastic system or of the original stochastic delay equation.

This boundary corresponds to the creation or disappearance of a positive interior maximum of the stationary amplitude density and therefore characterizes a qualitative change in the most probable stochastic amplitude.

3.4.3. Local state classification and transition ordering

For $\sigma > 0$, the local amplitude dynamics can be divided into three regimes according to μ_1/μ_3:

$$\begin{cases} 2\mu_1 < \mu_3, \quad \Lambda_{\mathrm{proj}} < 0, \quad \delta_0 \text{ is an attracting invariant probability measure,} \\ \mu_3 < 2\mu_1 < 2\mu_3, \quad p_s \text{ is normalizable but has no interior maximum for } r > 0, \\ \mu_1 > \mu_3, \quad p_s \text{ has a unique interior maximum at } r_{\mathrm{mp}} > 0. \end{cases} \tag{56}$$

The equalities $2\mu_1 = \mu_3$ and $\mu_1 = \mu_3$ correspond to the D- and P-type transition thresholds, respectively.

Within the truncated local model, solving the two threshold relations for the delay at a fixed noise intensity gives

$$\tau_{D,\mathrm{proj}}(\sigma) = \tau_c + \frac{q_r/2 - \kappa_r}{\chi}\sigma^2. \tag{57}$$

$$\tau_{P,\mathrm{proj}}(\sigma) = \tau_c + \frac{q_r - \kappa_r}{\chi}\sigma^2. \tag{58}$$

These equalities belong to the truncated projection model; they are not asserted as asymptotic boundary expansions for the full SGK stochastic system or for the original stochastic delay equation.

If $d_r = q_r/2 - \kappa_r > 0$, then $\tau_{D,\mathrm{proj}}(\sigma) < \tau_{P,\mathrm{proj}}(\sigma)$. Thus, at fixed noise intensity, increasing the delay causes the auxiliary projection model to cross the D-type transition boundary before the P-type transition boundary. Conversely, for a fixed $\tau > \tau_c$, $\sigma_{P,\mathrm{proj}}(\tau) < \sigma_{D,\mathrm{proj}}(\tau)$. Therefore, as the noise intensity increases, the stationary density first loses its positive-amplitude interior peak, after which the zero state becomes sample-wise exponentially stable.

3.4.4. Numerical definitions for the full Nth-order SGK stochastic system

The preceding boundaries are obtained from the auxiliary direct center-projection model and describe only the leading-order local stochastic dynamics in a neighborhood of the Hopf point. Although $\boldsymbol{L}_j$ preserves the complex structure, it generally does not leave the two-dimensional center subspace invariant. Stochastic feedback from the stable modes can therefore shift the actual boundaries of the full Nth-order SGK stochastic system.

The stochastic variational equation of the full Nth-order SGK stochastic system at the origin is

$$\mathrm{d}\boldsymbol{\xi}(t) = \boldsymbol{A}_{\mathrm{SGK}}(\tau)\boldsymbol{\xi}(t)\,\mathrm{d}t + \sigma \sum_{j=1}^{4} \boldsymbol{L}_j \boldsymbol{\xi}(t)\,\mathrm{d}W_j(t), \qquad \boldsymbol{\xi}(0) \neq \mathbf{0}. \tag{59}$$

Its maximal Lyapunov exponent is defined as

$$\Lambda_{\max}^{(N)}(\tau,\sigma) = \limsup_{t\to\infty} \frac{1}{t} \ln\|\boldsymbol{\xi}(t)\|. \tag{60}$$

Accordingly, the numerical D-transition set of the full Nth-order SGK stochastic system is defined by

$$\Gamma_{D,N} = \left\{(\tau,\sigma) : \Lambda_{\max}^{(N)}(\tau,\sigma) = 0,\ \Lambda_{\max}^{(N)} \text{ changes sign across the point}\right\}. \tag{61}$$

For a prescribed τ, if the maximal Lyapunov exponent changes from positive to negative for the first time as σ increases, define

$$\sigma_{D,N}(\tau) = \inf\left\{\sigma > 0 : \Lambda_{\max}^{(N)}(\tau,\sigma) \le 0\right\}. \tag{62}$$

For the full Nth-order SGK stochastic system, the numerical signature of a P-type transition is taken to be the stationary marginal density of the center amplitude along nonlinear stochastic trajectories. Let

$$r_{c,N}(t) = |\boldsymbol{u}^* \boldsymbol{Y}(t)|, \tag{63}$$

and denote its stationary marginal density by $p_{c,N}(r;\tau,\sigma)$. A P-type transition in the probability-density sense is identified when the number of interior maxima of $p_{c,N}$ on $r > 0$ changes, or when a nonzero interior peak collapses to the zero-amplitude boundary. The projected indicators (55) and (51) are used as local theoretical predictions for the P- and D-type transition indicators of the full Nth-order SGK stochastic system, respectively. Their actual locations must be verified numerically by stationary-density statistics and maximal-Lyapunov-exponent calculations.

4. Delay tuning of the quarter-cycle rhythm under P–D transition constraints

4.1. Deterministic quarter-cycle periodic branch and stability interval

For the selected full $N = 8$ SGK system, let the deterministic quarter-cycle periodic solution be denoted by $\boldsymbol{Y}_p(t;\tau) = \boldsymbol{Y}_p(t + T_\tau;\tau)$, where T_τ is the period. Introducing $s = t/T_\tau \in [0, 1]$, the periodic solution satisfies the boundary-value problem

$$\frac{\mathrm{d}\boldsymbol{Y}_p}{\mathrm{d}s} = T_\tau \boldsymbol{\mathcal{F}}(\boldsymbol{Y}_p, \tau), \qquad \boldsymbol{Y}_p(0;\tau) = \boldsymbol{Y}_p(1;\tau). \tag{64}$$

To remove the nonuniqueness caused by time translation in the autonomous system, the phase condition

$$\int_0^1 \left\langle \boldsymbol{Y}_p(s;\tau) - \boldsymbol{Y}_{\mathrm{ref}}(s), \frac{\mathrm{d}\boldsymbol{Y}_{\mathrm{ref}}}{\mathrm{d}s}(s) \right\rangle \mathrm{d}s = 0 \tag{65}$$

is imposed, where $\boldsymbol{Y}_{\mathrm{ref}}$ is the reference solution from the adjacent continuation step. Starting from the small-amplitude periodic solution supplied by the Hopf normal form, Eqs (64) and (65) can be solved continuously along the quarter-cycle branch by using τ as the continuation parameter.

The variational equation along the periodic solution is $\dot{\boldsymbol{\xi}}(t) = D_{\boldsymbol{Y}}\boldsymbol{\mathcal{F}}(\boldsymbol{Y}_p(t;\tau), \tau)\boldsymbol{\xi}(t)$. Let the fundamental solution matrix $\boldsymbol{\Phi}(t;\tau)$ satisfy

$$\dot{\boldsymbol{\Phi}}(t;\tau) = D_{\boldsymbol{Y}}\boldsymbol{\mathcal{F}}(\boldsymbol{Y}_p(t;\tau), \tau)\boldsymbol{\Phi}(t;\tau), \qquad \boldsymbol{\Phi}(0;\tau) = \boldsymbol{I}_{64}. \tag{66}$$

The monodromy matrix is $\boldsymbol{M}(\tau) = \boldsymbol{\Phi}(T_\tau;\tau)$. Its eigenvalues $\varrho_j(\tau)$ are the Floquet multipliers. Because the system is autonomous, the trivial multiplier $\varrho_1 = 1$ associated with time translation is always present. Define the modulus of the largest nontrivial multiplier by

$$\rho_F^{(8)}(\tau) = \max_{j\geq 2} |\varrho_j(\tau)|. \tag{67}$$

The quarter-cycle periodic solution is locally asymptotically stable in transverse directions when $\rho_F^{(8)}(\tau) < 1$. The right stability boundary is defined as

$$\tau_R^{(8)} = \inf\left\{\tau > \tau_c^{(8)} : \rho_F^{(8)}(\tau) = 1\right\}. \tag{68}$$

If the periodic branch terminates before a nontrivial multiplier reaches the unit circle, the dynamical mechanism of the branch termination must be determined by numerical continuation. The deterministic stable quarter-cycle interval is

$$I_{\mathrm{det}}^{(8)} = (\tau_c^{(8)}, \tau_R^{(8)}). \tag{69}$$

Its left endpoint is determined by the Hopf bifurcation of the equilibrium, whereas its right endpoint is determined by the Floquet stability of the periodic branch.

4.2. Quarter-cycle parameter domain under stochastic transition constraints

For $\tau \in I_{\mathrm{det}}^{(8)}$, the full $N = 8$ deterministic SGK system possesses a stable periodic branch connected to the critical quarter-cycle mode. The auxiliary direct center-projection model predicts the ordering of the two local stochastic mechanisms, but the boundaries used for parameter selection are obtained numerically from the full $N = 8$ SGK stochastic system.

Based on the maximal Lyapunov exponent, define the basic stochastic domain

$$\mathcal{D}_{D,8} = \left\{(\tau, \sigma) : \tau \in I_{\mathrm{det}}^{(8)},\ \Lambda_{\max}^{(8)}(\tau, \sigma) > 0\right\}. \tag{70}$$

When a single sign-changing D boundary exists, this becomes $0 \le \sigma < \sigma_{D,8}(\tau)$.

The P transition is reported as a numerical bracket $[\sigma_{P,8}^{-}(\tau), \sigma_{P,8}^{+}(\tau)]$, not as a statistical confidence interval. Define the representative midpoint

$$\sigma_{P,8}^{\mathrm{mid}}(\tau) = \frac{\sigma_{P,8}^{-}(\tau) + \sigma_{P,8}^{+}(\tau)}{2}. \tag{71}$$

The lower, midpoint, and upper envelopes provide conservative, nominal, and optimistic descriptions of the density-based limit. For $e \in \{-, \mathrm{mid}, +\}$, define

$$\mathcal{D}_{\mathrm{rob},8}^{e} = \left\{(\tau, \sigma) : \tau \in I_{\mathrm{det}}^{(8)},\ 0 \le \sigma < \min\{\sigma_{P,8}^{e}(\tau), \sigma_{D,8}(\tau)\}\right\}. \tag{72}$$

The lower-envelope domain $\mathcal{D}_{\mathrm{rob},8}^{-}$ is used for conservative design, whereas the midpoint domain is the nominal summary. The upper envelope is retained only to display the numerical bracket uncertainty. Neither the P-density condition nor the D-boundary condition alone guarantees the target phase relation; finite-amplitude simulations must additionally satisfy the phase-error and valid-amplitude criteria.

4.3. Delay-tuning criterion at a prescribed noise level

For a prescribed noise upper bound $\bar{\sigma}$, define the D-constrained delay set

$$I_{D,8}(\bar{\sigma}) = \left\{\tau \in I_{\mathrm{det}}^{(8)} : \bar{\sigma} < \sigma_{D,8}(\tau)\right\}. \tag{73}$$

For each P-envelope choice $e \in \{-, \mathrm{mid}, +\}$, define

$$\begin{aligned} I_{P,8}^{e}(\bar{\sigma}) &= \left\{\tau \in I_{\mathrm{det}}^{(8)} : \bar{\sigma} < \sigma_{P,8}^{e}(\tau)\right\}, \\ I_{\mathrm{walk},8}^{e}(\bar{\sigma}) &= \left\{\tau \in I_{D,8}(\bar{\sigma}) \cap I_{P,8}^{e}(\bar{\sigma}) : E_{\phi}(\tau, \bar{\sigma}) \le \varepsilon_{\phi}\right\}. \end{aligned} \tag{74}$$

When one grid point must be selected, the envelope-dependent joint margin is

$$M_{PD,8}^{e}(\tau; \bar{\sigma}) = \min\left\{\sigma_{P,8}^{e}(\tau) - \bar{\sigma},\ \sigma_{D,8}(\tau) - \bar{\sigma}\right\}, \qquad e \in \{-, \mathrm{mid}, +\}. \tag{75}$$

The conservative grid recommendation maximizes $M_{PD,8}^{-}$ over the sampled delays satisfying the phase criterion. This is a discrete-grid recommendation and is not presented as a global continuous optimum. The numerical boundaries, envelope interpolation, feasible intervals, and margins are evaluated in Section 5.

5. Numerical validation and dynamical mechanisms

5.1. Original deterministic DDE: Identification of the delay-induced quarter-cycle critical mode

The critical-spectrum calculation in this subsection is performed directly for the original deterministic DDE, obtained from Eq (2) by setting $\sigma = 0$. Fixing $K_c = 0.1$ and $\omega_0 = 2.0$, candidate dimensionless parameter sets with different values of the linear growth rate α are compared. The selection jointly considers uniqueness of the critical conjugate pair, the transversality coefficient, the noncritical spectral gap, consistency of the quarter-cycle mode, and the continuation range of the periodic branch. The preliminary branch width in the final column is the delay length over which the screening continuation retains a stable target-mode periodic solution; it is used only for parameter screening. The results are listed in Table 1.

Table 1. Candidate parameters and Hopf characteristics.

Group	α	K_c	ω_0	τ_c^{DDE}	Ω_c^{DDE}	χ	Prelim. branch width
1	0.0050	0.100	2.000	2.163635	2.031225	0.04350	0.40530
2	0.0075	0.100	2.000	2.121018	2.037997	0.05387	0.31273
3	0.0100	0.100	2.000	2.085234	2.043589	0.06278	0.24330
4	0.0125	0.100	2.000	2.053800	2.048412	0.07075	0.17388

Group 1 has the largest noncritical spectral gap and the widest preliminary stability interval. Therefore, the subsequent calculations use $\alpha = 0.005$, $K_c = 0.1$, and $\omega_0 = 2.0$. The cyclic spatial-mode decomposition of the original deterministic DDE gives $\tau_c^{\mathrm{DDE}} = 2.1636345421$ and $\Omega_c^{\mathrm{DDE}} = 2.0312249900$.

The residual of the critical root is 1.84×10^{-16}, the largest real part among the noncritical eigenvalues is -0.0357, and the transversality coefficient is $\chi = 0.043504$. The critical spatial mode corresponds to the ring eigenvalue $\rho = -\mathrm{i}$ and has a $\pi/2$ phase difference between neighboring oscillators, thereby satisfying the numerical spectral condition for the quarter-cycle Hopf mode.

5.2. Deterministic SGK convergence and preservation of the quarter-cycle critical dynamics

The matrix $\boldsymbol{A}_{\mathrm{SGK}}(\tau)$ is reassembled using the Koornwinder endpoint values, orthogonality relations, derivative expansion, and current- and delayed-endpoint reconstruction formulas given in Section 2. Algebraic self-checks confirm $K_p(1) = 1$, $K_p(-1) = \kappa_p$, and an $8N \times 4$ diffusion matrix; no independent noise source is introduced for each of the $8N$ state components. The critical-branch diagnostics for different truncation orders are summarized in Table 2.

Table 2. Critical-branch diagnostics by SGK order.

N	Dimension	$\tau_c^{(N)}$	$\Omega_c^{(N)}$	Branch diagnosis	Decision
3	24	–	–	Competing crossings	Rejected
4	32	–	–	Competing crossings	Rejected
5	40	2.605161	2.126475	Incorrect critical branch	Rejected
6	48	–	–	Incorrect mode	Rejected
7	56	2.151888	2.032417	Target branch; low accuracy	Rejected
8	64	2.161156	2.031711	Target branch	Accepted
9	72	2.163895	2.031197	Target branch	Accepted
10	80	2.163673	2.031217	Target branch	Accepted

Table 2 identifies whether each truncation preserves the intended critical branch. The quantitative errors of the tested branches are then reported in Table 3. Here $e_\tau = 100|\tau_c^{(N)} - \tau_c^{\mathrm{DDE}}|/\tau_c^{\mathrm{DDE}}$ and $e_\Omega = 100|\Omega_c^{(N)} - \Omega_c^{\mathrm{DDE}}|/\Omega_c^{\mathrm{DDE}}$. For the common periodic benchmark used in Figure 1, e_A and e_f are the relative errors of the mean oscillation amplitude and frequency, E_X is the normalized one-period physical-state error, E_H is the normalized history-segment reconstruction error in the Koornwinder history norm, and E_ϕ is the one-period mean of the phase error defined in Eq (4).

Trajectory comparisons use a common phase origin before the norms are evaluated; the resulting errors are listed in Table 3.

Table 3. Deterministic SGK errors relative to the original DDE.

N	e_τ (%)	e_Ω (%)	e_A (%)	e_f (%)	E_X (%)	E_H (%)	E_ϕ
5	20.4067	4.6893	99.6383	1.2986	99.8688	99.5871	1.924
7	0.5429	0.0587	9.3529	0.0419	10.7412	9.0852	1.21×10^{-14}
8	0.1145	0.0239	2.1191	0.0051	2.2075	2.0712	5.98×10^{-15}
9	0.0120	0.0014	0.2213	8.76×10^{-4}	0.2452	0.2157	1.91×10^{-14}
10	0.0018	3.71×10^{-4}	0.0348	8.84×10^{-5}	0.0364	0.0340	1.06×10^{-14}

The screening requirements are $e_\tau < 0.2\%$, $e_\Omega < 0.05\%$, $e_A < 3\%$, $e_f < 0.01\%$, $E_X < 3\%$, and $E_H < 3\%$. When these left-Hopf and benchmark-reconstruction thresholds are varied uniformly by $\pm 20\%$, $N = 8$ remains the lowest tested passing order for this parameter set. It is therefore adopted as the principal computational compromise, not as a proof of uniform truncation accuracy over the entire periodic window. The $N = 9$ and $N = 10$ systems are used to check selected stochastic estimates and the right endpoint of the periodic branch.

The time-domain response and history-segment reconstruction used to support this order selection are compared in Figure 1. Time and history coordinates are normalized by $T_0 = 2\pi/\omega_0$ and τ, respectively. The insets resolve the output peak and the pointwise history error $e_N(\theta)$.

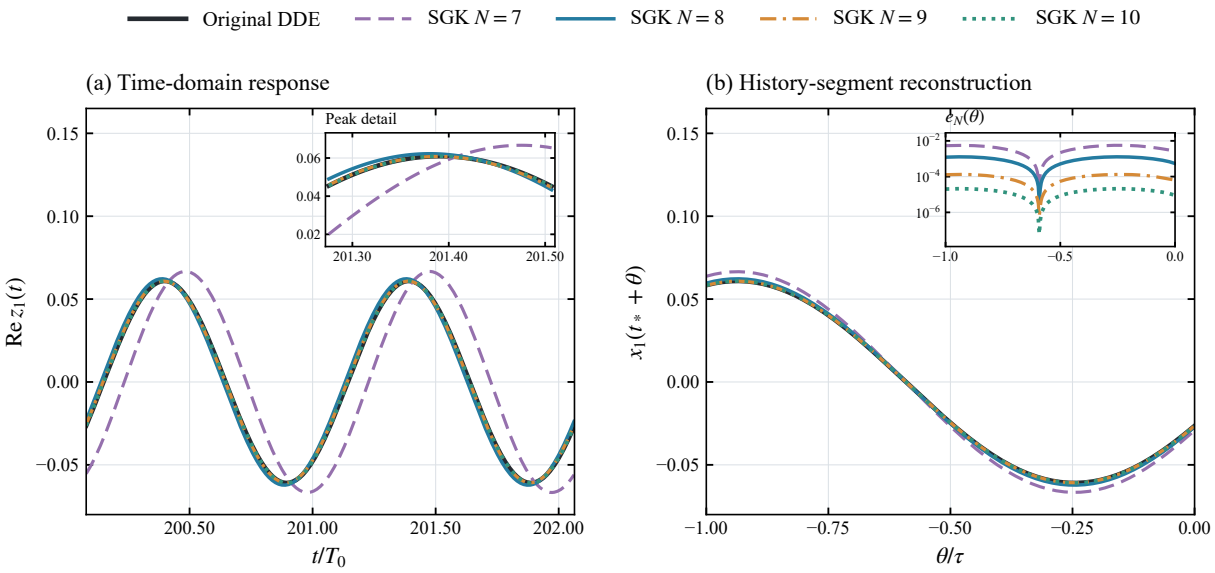


Figure 1. Deterministic DDE and SGK comparison: (a) oscillator output and peak detail; (b) history reconstruction and pointwise error. Orders $N = 7, 8, 9, 10$ are compared.

Figure 1 shows visible amplitude and phase deviations for $N = 7$, whereas the $N = 8$, 9, and 10 results nearly coincide with the original deterministic DDE. The history-segment error also decreases rapidly with increasing order. These results provide a deterministic accuracy basis for the subsequent branch and stochastic-dynamics calculations using the $N = 8$ system.

5.3. Full $N = 8$ SGK periodic window and direct DDE rotating-wave validation

Five delay values to the right of the Hopf point are selected to compare the analytical rotating-wave relation of the quarter-cycle phase pattern with periodic solutions of the original deterministic DDE. Substitution of $z_j(t) = R\exp\{\mathrm{i}[\Omega t + (j-1)\pi/2]\}$ into the original deterministic DDE gives the corresponding rotating-wave algebraic relation. Let $T_0 = 2\pi/\omega_0$ denote the uncoupled-oscillator period and $\Delta\tau = \tau - \tau_c^{\mathrm{DDE}}$. The values R_{RW} and Ω_{RW} in Table 4 are obtained from the rotating-wave relation rather than from an artificially scaled normal-form curve. The mean and maximum relative amplitude errors are 7.33×10^{-6} and 1.80×10^{-5}, respectively; the mean and maximum relative angular-frequency errors are 2.35×10^{-9} and 3.39×10^{-9}, respectively.

Table 4. Rotating-wave predictions and direct DDE validation.

$\Delta\tau/T_0$	τ	R_{RW}	R^{DDE}	e_R	Ω_{RW}	e_Ω
0.010	2.195050	0.038905299	0.038905998	1.80×10^{-5}	2.026174811	2.75×10^{-9}
0.020	2.226466	0.052446996	0.052446774	4.23×10^{-6}	2.021090356	3.39×10^{-9}
0.030	2.257882	0.060944384	0.060944044	5.59×10^{-6}	2.015984467	2.77×10^{-9}
0.040	2.289298	0.066389197	0.066388892	4.59×10^{-6}	2.010869401	1.86×10^{-9}
0.050	2.320714	0.069528085	0.069527786	4.30×10^{-6}	2.005756873	9.85×10^{-10}

Figure 2 presents the rotating-wave reconstruction at $\tau = 2.463620$ and the SGK-order errors used in

the truncation comparison.

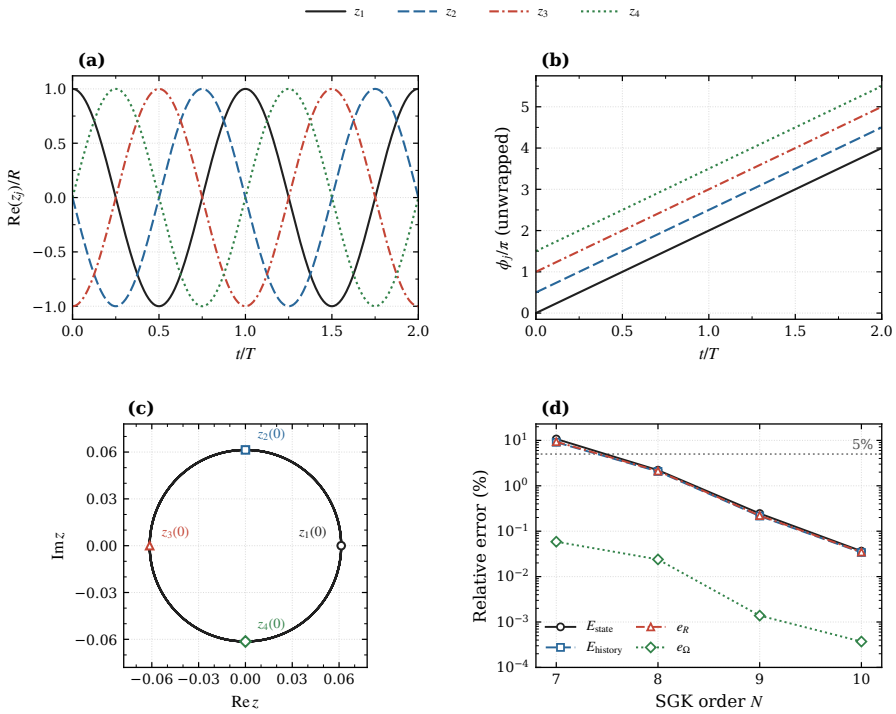


Figure 2. Quarter-cycle reconstruction and SGK accuracy: (a) normalized waveforms; (b) unwrapped phases; (c) common complex-plane orbit; (d) relative state, history, amplitude, and critical-frequency errors.

In Figure 2(a)–(c), the four oscillators have equal amplitudes and frequencies, while their unwrapped phases differ successively by $\pi/2$. Their initial states lie one quarter of a circumference apart on the common orbit. Panel (d) shows the decrease in the four displayed relative errors with increasing order. The critical-mode phase errors are near numerical round-off and are therefore excluded from the percentage axis. The plotted interval spans two periods, and the orbit markers indicate the four states at $t = 0$. The 5% reference applies to state, history, and amplitude errors. Panels (a)–(c) reconstruct a rotating wave rather than an independent transient simulation.

The direct DDE calculations above validate the rotating-wave algebraic structure but do not define the complete stochastic operating region. For the full $N = 8$ deterministic SGK system, the periodic branch is continued over the delay parameter. Using the group symmetry of the quarter-cycle rotating wave, the variational equation along the periodic orbit is transformed into a constant-coefficient real linear system in rotating coordinates, from which the Floquet exponents are computed directly.

Representative results are listed in Table 5.

Table 5. Floquet diagnostics along the $N = 8$ SGK branch.

τ	T_τ	Ω	R	$\rho_F^{(8)}$	Re $\nu_{\max}$	Stability
2.200000	3.102087	2.025470	0.043249	0.990501	-3.08×10^{-3}	Stable
2.300000	3.127152	2.009236	0.069005	0.976099	-7.74×10^{-3}	Stable
2.400000	3.152524	1.993065	0.070508	0.975067	-8.01×10^{-3}	Stable
2.463620	3.168575	1.982969	0.061376	0.981013	-6.05×10^{-3}	Stable
2.500000	3.177659	1.977300	0.051254	0.986697	-4.22×10^{-3}	Stable
2.530000	3.185075	1.972696	0.038022	0.992643	-2.32×10^{-3}	Stable
2.548255	3.189549	1.969929	0.024937	0.996824	-9.97×10^{-4}	Stable
2.560000	3.192410	1.968164	0.007094	0.999742	-8.07×10^{-5}	Stable

In Figure 3(a), the dotted curve is the algebraic DDE relation and the open circles mark sampled endpoints; this reference is not a time-domain integration. Figure 3 compares the amplitude branches and nontrivial Floquet multiplier moduli for $N = 8, 9, 10$; Table 5 retains representative $N = 8$ periods, angular frequencies, and critical Floquet exponents.

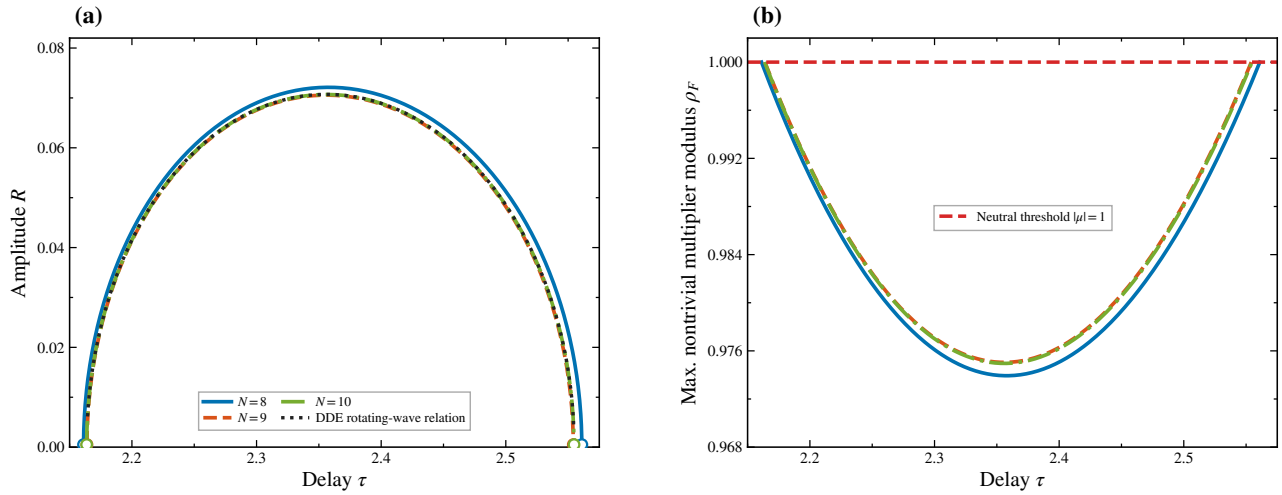


Figure 3. Deterministic SGK branches for $N = 8, 9, 10$: (a) amplitude and algebraic DDE reference; (b) largest nontrivial Floquet multiplier modulus, with neutral threshold $\rho_F = 1$.

Figure 3(b) shows that $\rho_F^{(8)} < 1$ in the branch interior, consistent with the negative critical exponents in Table 5. As the right endpoint is approached, the periodic amplitude tends to zero, $\rho_F^{(8)} \to 1$, and Re $\nu_{\max} \to 0^-$. Hence, the right boundary is not an independent Floquet instability of a finite-amplitude periodic orbit; rather, the quarter-cycle periodic branch reconnects to the equilibrium branch at a second Hopf point. The right endpoints obtained with different truncation orders are $\tau_R^{(8)} = 2.5610033$, $\tau_R^{(9)} = 2.5541681$, and $\tau_R^{(10)} = 2.5547391$.

The stochastic calculations for the full $N = 8$ SGK stochastic system therefore use the deterministic interval

$$I_{\text{det}}^{(8)} = (2.1611565,\ 2.5610033).$$

To complement the branch diagnostics, Figure 4 shows representative deterministic DDE responses at $\tau = 2.18$, 2.40, and 2.50, starting from the prescribed perturbed rotating-wave histories. The real and

imaginary components exhibit an initial amplitude adjustment followed by sustained oscillations over the displayed interval.

The phase-plane trajectories in Figure 4 approach nearly circular loops over the displayed time window. These finite-time responses illustrate the selected histories; they do not establish global attraction or replace the SGK Floquet calculation. In the phase planes, open orange and filled blue markers identify the first and last saved numerical points.

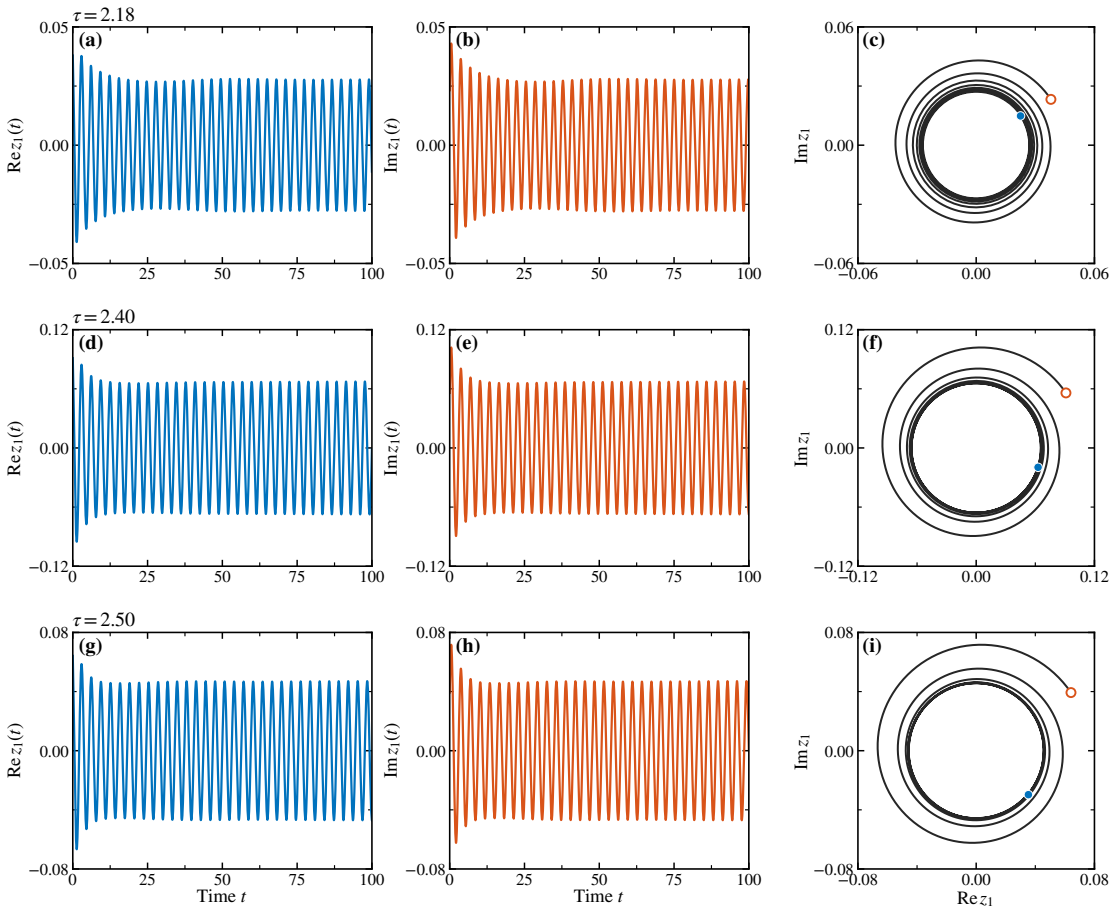


Figure 4. Deterministic DDE responses at $\tau = 2.18$, 2.40, and 2.50 (top to bottom). Columns show $\mathrm{Re}\, z_1(t)$, $\mathrm{Im}\, z_1(t)$, and complex-plane trajectories over $0 \le t \le 100$.

5.4. Auxiliary projection indicators and full $N = 8$ SGK stochastic boundaries

This subsection first evaluates the auxiliary direct center-projection indicators and then computes the stochastic transition brackets and D-boundary estimates for the full $N = 8$ SGK stochastic system. No stochastic boundary reported below is claimed as a directly computed boundary of the original infinite-dimensional stochastic delay equation.

5.4.1. Auxiliary projection coefficients and spectral-continuation indicators

The critical right and left eigenvectors are normalized by $\boldsymbol{u}^*\boldsymbol{v} = 1$. Owing to symmetry, the four noise channels have identical projection coefficients. For $N = 8$, $\gamma_j = 0.20683954 - 0.01181354\,\mathrm{i}$ for

$j = 1, \ldots, 4$.

The counter-rotating projection coefficients δ_j are of order 10^{-15}. The convergence of the combined coefficients with respect to the SGK order is shown in Table 6.

Table 6. Auxiliary radial-equation coefficients.

N	q_r	q_θ	κ_r	κ_θ	$d_r = q_r/2 - \kappa_r$	$q_r - \kappa_r$
8	0.171130	5.5824×10^{-4}	2.7912×10^{-4}	0.009774	0.085286	0.170851
9	0.170952	5.3472×10^{-4}	2.6736×10^{-4}	0.009561	0.085209	0.170685
10	0.170939	5.3649×10^{-4}	2.6825×10^{-4}	0.009576	0.085201	0.170671

The linearized growth term underlying the auxiliary projection yields only a local asymptotic boundary near the left Hopf point. To compare predictions over the entire deterministic periodic interval, let $\beta_8(\tau)$ denote the real part of the leading eigenvalue of $\boldsymbol{A}_{\mathrm{SGK}}(\tau)$, and define the continuation-type predictions based on the full linear spectrum by

$$\widehat{\sigma}_{P,\mathrm{proj}}(\tau) = \sqrt{\frac{\beta_8(\tau)}{q_r - \kappa_r}}, \qquad \widehat{\sigma}_{D,\mathrm{proj}}(\tau) = \sqrt{\frac{\beta_8(\tau)}{q_r/2 - \kappa_r}}. \tag{76}$$

These predictions vanish at both the left and right Hopf points and describe the arch-shaped trend across the full interval. They are not equivalent to the square-root asymptotic expressions derived at the left endpoint in Section 3.

Figure 5 illustrates the probability-density shapes in the three noise regimes. Below the auxiliary P-type threshold, the radial density has an interior peak at a positive amplitude. Between the auxiliary P- and D-type thresholds, the density maximum shifts to the zero-amplitude boundary while the center Lyapunov exponent remains positive. After the auxiliary D-type threshold is crossed, finite-time samples progressively concentrate near the zero state.

The three probability-density regimes predicted by the auxiliary direct center-projection model are displayed in Figure 5.

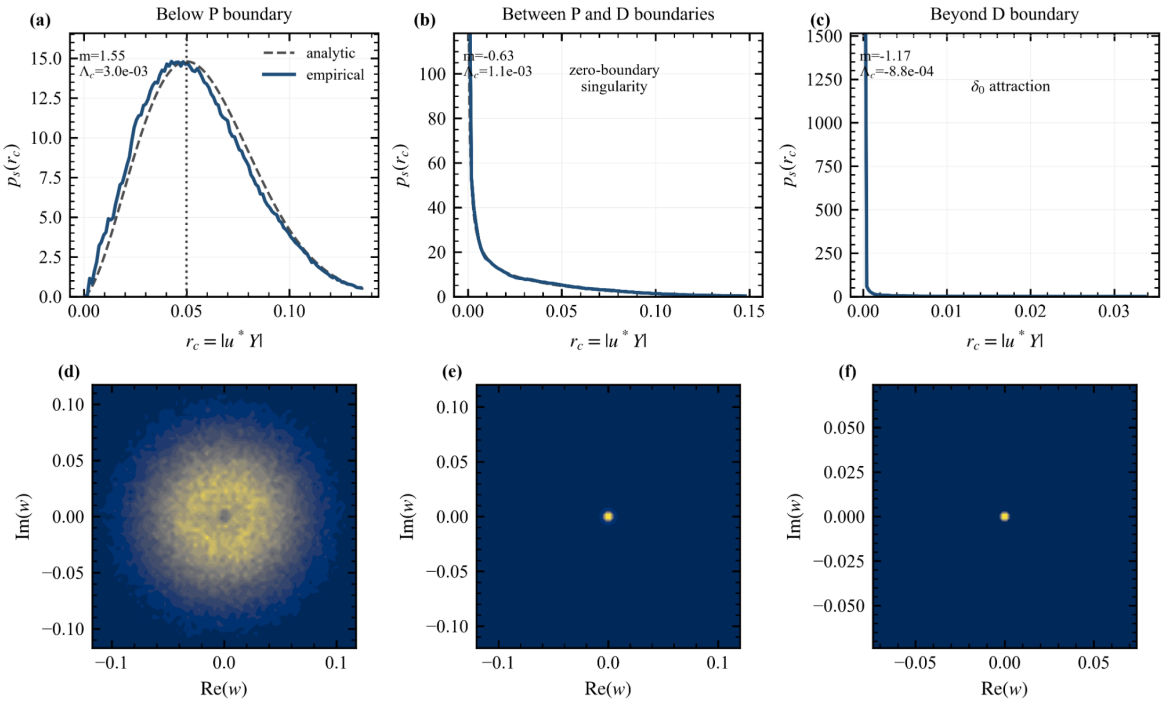


Figure 5. Auxiliary direct center-projection dynamics in the three regimes: (a)–(c) stationary amplitude densities; (d)–(f) joint center-plane densities.

5.4.2. P-transition brackets for the full $N = 8$ SGK stochastic system

For the full nonlinear $N = 8$ SGK stochastic system, the center amplitude is sampled as $r_{c,8} = |\boldsymbol{u}^*\boldsymbol{Y}|$. The numerical integration uses a splitting scheme consisting of a rotating linear subflow, a cubic dissipative subflow, and a multiplicative-noise subflow; both the linear and stochastic subflows are advanced exactly. The main scan uses $\Delta t = 0.02$ and is checked at representative points by halving the step size and extending the statistical window. Here $Q_{0.995}$ is the empirical 99.5th percentile of the pooled retained $r_{c,8}$ samples at the corresponding parameter point. On $[0, Q_{0.995}]$, the stationary density is estimated jointly by equal-width bins and a boundary-corrected kernel-density estimator. A P-type transition is identified when the positive-amplitude interior peak collapses to the zero boundary.

The simulation and classification protocol is summarized in Table 7, and the resulting six $N = 8$ transition brackets are listed in Table 8.

Table 7. P-transition density-classification protocol.

Item	Numerical specification
Integrator and main step	Exact linear and multiplicative-noise subflows with a cubic dissipative subflow; main step $\Delta t = 0.02$, with representative endpoint checks at $\Delta t = 0.01$.
Long-time record	Anchor runs use total time 28,000, burn-in 12,000, statistical time 16,000, sampling interval 0.5, and 32,000 retained samples per realization.
Replicates and seeds	Deterministic seed rule recorded for every realization; two to four anchor replicates per (N, τ, σ), with adaptive extension when the density geometry is ambiguous.
Density estimators	Equal-width histogram and boundary-corrected KDE on $[0, Q_{0.995}]$; KDE bandwidth and the factors 0.8, 1.0, and 1.2 are recorded.
Classification	Interior peak, boundary dominated, or transition/ambiguous. Histogram and KDE geometry, mode location, block stationarity, and pooled classification are reported separately.
Uncertainty interpretation	$[\sigma^-_{P,8}, \sigma^+_{P,8}]$ is a numerical transition bracket between sampled noise levels, not a confidence interval.

The protocol in Table 7 separates density classification from uncertainty assessment: Disagreement between density estimators or insufficient stationarity is retained as a transition or ambiguous classification. Table 8 applies this rule at each sampled delay. Its lower and upper endpoints delimit sampled interior-peak and boundary-dominated states, respectively; intermediate samples are listed explicitly so that the width of each bracket can be interpreted against the underlying classifications.

Table 8. Full $N = 8$ SGK P-transition classifications.

τ	$\widehat{\sigma}_{P,\mathrm{proj}}$	$\sigma^-_{P,8}$	Transition samples	$\sigma^+_{P,8}$	$[\sigma^-_{P,8}, \sigma^+_{P,8}]$
2.20	0.0949	0.090	–	0.100	[0.090, 0.100]
2.25	0.1324	0.125	0.130, 0.135, 0.140	0.145	[0.125, 0.145]
2.30	0.1507	0.130	0.140, 0.150	0.160	[0.130, 0.160]
2.35	0.1570	0.160	0.170	0.180	[0.160, 0.180]
2.40	0.1533	0.150	–	0.155	[0.150, 0.155]
2.50	0.1111	0.100	0.110, 0.120	0.130	[0.100, 0.130]

Long-time simulations of the full $N = 8$ SGK stochastic system yield the final P-transition brackets $[0.090, 0.100]$, $[0.125, 0.145]$, $[0.130, 0.160]$, $[0.160, 0.180]$, $[0.150, 0.155]$, and $[0.100, 0.130]$ for $\tau \in \{2.20, 2.25, 2.30, 2.35, 2.40, 2.50\}$, respectively. Transition or ambiguous density states are observed at $\sigma = 0.130, 0.135, 0.140$ for $\tau = 2.25$; at $\sigma = 0.140, 0.150$ for $\tau = 2.30$; at $\sigma = 0.170$ for $\tau = 2.35$; and at $\sigma = 0.110, 0.120$ for $\tau = 2.50$. No additional transition point is required at $\tau = 2.20$ or 2.40. Every interval endpoint retains the same density classification when the time step is reduced from $\Delta t = 0.02$ to 0.01, so all six intervals are adopted as sampled-grid N=8 P-transition brackets under the stated protocol.

The updated full $N = 8$ SGK P-transition brackets preserve the arch-shaped increase-then-decrease dependence on τ predicted by spectral continuation. Their midpoints may lie slightly above or below the local prediction, rather than showing a systematic one-sided displacement. This difference is attributable

to finite-amplitude effects and stochastic feedback from stable modes; therefore, the local expression is retained as a neighborhood and trend prediction, whereas the long-time full $N = 8$ SGK brackets are used for the final parameter classification.

Representative higher-order anchor calculations were performed at two delays. The low-noise and high-noise anchors were chosen on opposite sides of the corresponding $N = 8$ P bracket. Table 9 lists the four paired $N = 9$ and $N = 10$ density checks. The low-noise anchors retain an interior peak and the high-noise anchors are boundary dominated, while the reported stationarity and replicate warnings prevent these checks from being interpreted as complete high-order P brackets.

Table 9. P-density checks at $N = 9$ and $N = 10$.

τ	σ	Anchor role	Pooled $N = 9/N = 10$ geometry	Assessment
2.35	0.150	Low	Interior peak / interior peak	Yes, with stationarity warning
2.35	0.190	High	Boundary dominated / boundary dominated	Yes, with stationarity warning
2.50	0.090	Low	Interior peak / interior peak	Yes
2.50	0.140	High	Boundary dominated / boundary dominated	Yes, with replicate warning

The evolution of the full $N = 8$ SGK center-amplitude density at $\tau = 2.35$ is shown in Figure 6.

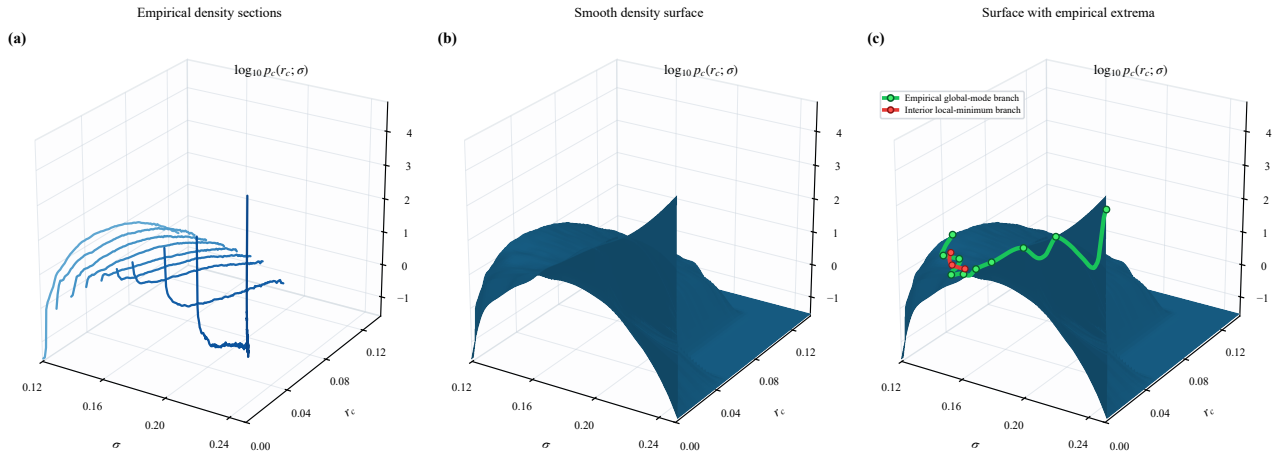


Figure 6. Full $N = 8$ SGK densities at $\tau = 2.35$: (a) empirical sections; (b) interpolated display surface; (c) sampled global modes (green) and local minima (red). Vertical axes show $\log_{10} p_c(r_c;\sigma)$.

Figure 6(a) displays the sampled density sections, while panels (b) and (c) summarize their geometry and empirical extrema. The smooth surface between sampled noise levels and the tapered low-density tails introduce no additional simulation data. The final P classification remains based on the sampled full $N = 8$ SGK densities and the diagnostics in Table 8, rather than on the appearance of the interpolated surface. The display uses shape-preserving interpolation, a density floor of 0.03, and tail tapering. Curves joining the extrema are visual guides, not computed continuous bifurcation branches.

To make the change in density geometry explicit, representative full $N = 8$ SGK densities from the three stochastic regimes are compared in Figure 7.

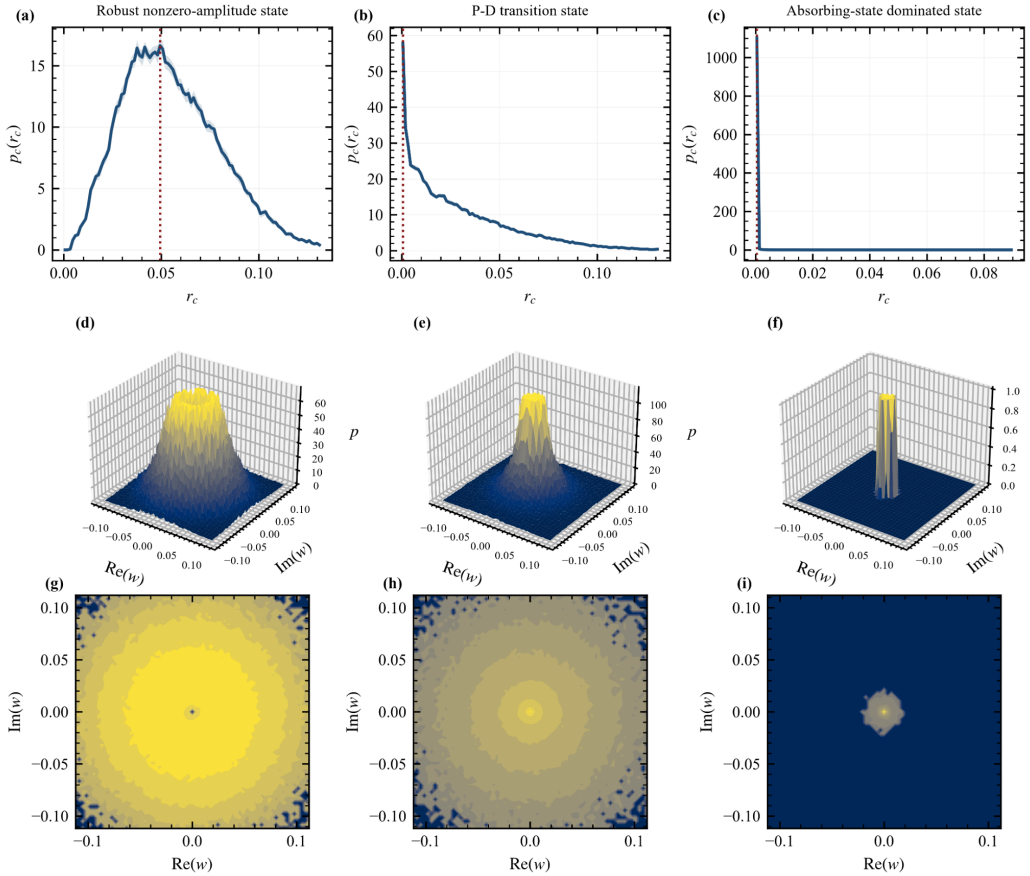


Figure 7. Full $N = 8$ SGK densities below the P bracket, between the P bracket and D estimate, and beyond the D estimate (left to right).

Figure 7 makes the two-stage transition explicit. The interior density peak is present below the P bracket, is lost in the intermediate P–D regime, and is replaced by concentration near the absorbing zero state beyond the D boundary.

5.4.3. D-boundary estimates for the full $N = 8$ SGK stochastic system

The stochastic variational system of the full $N = 8$ SGK approximation is integrated using an exact linear half-step, an exact multiplicative-noise step, and a second exact linear half-step. The perturbation vector is renormalized every 0.5 time units. The full $N = 8$ SGK D-boundary estimate is determined by a local linear regression of $\Lambda_{\max}^{(8)}$ against σ^2, and the confidence intervals at the positive- and negative-sign confirmation points lie on opposite sides of zero. With the exact linear subflow, the discrepancy between the numerical exponent at $\sigma = 0$ and the leading matrix eigenvalue is below 10^{-6}.

Table 10 summarizes the auxiliary projection predictions, full $N = 8$ SGK stochastic estimates, and sign-confirmation points.

Table 10. Full $N = 8$ SGK D-boundary estimates.

τ	$\widehat{\sigma}_{D,\mathrm{proj}}$	$\sigma_{D,8}$	Positive-sign σ	Negative-sign σ	Relative deviation
2.20	0.1344	0.1351	0.090	0.170	0.6%
2.25	0.1874	0.1839	0.150	0.230	1.9%
2.30	0.2132	0.1976	0.180	0.220	7.3%
2.35	0.2222	0.2154	0.190	0.250	3.1%
2.40	0.2170	0.2116	0.170	0.250	2.5%
2.45	0.1970	0.1949	0.150	0.230	1.1%
2.50	0.1573	0.156 [0.150, 0.161]	0.150	0.160	0.8%

As shown in Table 10, the fitted $N = 8$ D-boundary follows the spectral prediction over the computed delay range, with the largest relative deviation occurring at $\tau = 2.30$. The truncation-order comparison is reported in Table 11.

Table 11. Previously reported protocol-specific D-boundary fits.

τ	$\sigma_{D,8}$	$\sigma_{D,9}$	$\sigma_{D,10}$	Rel. diff. $N = 8$ vs. 10
2.30	0.1976	0.2038	0.2041	3.17%
2.50	0.1598	0.1513	0.1520	5.17%

Table 11 shows close agreement between the $N = 9$ and $N = 10$ fits at both representative delays, whereas the $N = 8$ value retains a visible protocol- and order-dependent deviation, especially at $\tau = 2.50$. The remaining sensitivity to statistical time and step size at $\tau = 2.30$ is documented in Table 12.

Table 12. D-boundary convergence checks at $\tau = 2.30$.

Δt	Statistical time	Realizations	$\sigma_{D,8}$	Description
0.02	4000	8	0.2185	Insufficient statistical window
0.02	6000	8	0.2076	Approaching long-time estimate
0.02	8000	8	0.1976	Reference estimate
0.01	6000	8	0.1984	Step-size check

The convergence data in Table 12, together with the P-transition intervals and SGK-order comparison, are assembled graphically in Figure 8.

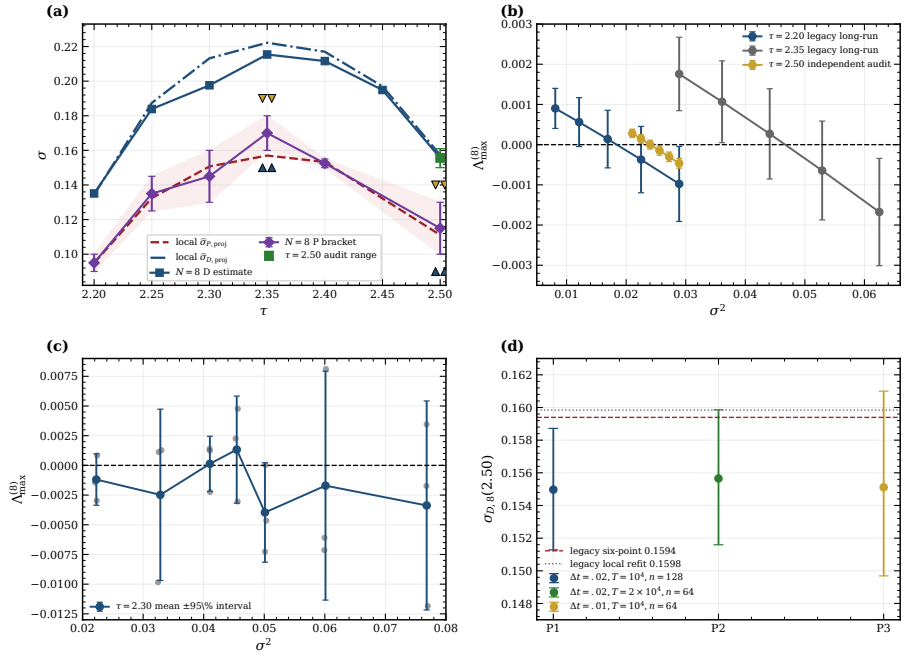


Figure 8. P brackets and SGK D diagnostics: (a) transition estimates; (b) Lyapunov scans; (c) seed diagnostics at $\tau = 2.30$; (d) protocol comparisons at $\tau = 2.50$.

In Figure 8, shading denotes the P bracket, the $\tau = 2.50$ error bar denotes the audit range, and connecting lines guide the eye. Figure 8 combines the sampled P brackets with the finite-order SGK D diagnostics. The $\tau = 2.50$ audit demonstrates that the two close previously reported fits do not by themselves establish convergence. Increasing the seed count, extending the statistical window, and halving the time step give stable central estimates near 0.155–0.156 but retain a non-negligible numerical range. All D values are therefore interpreted as local zero-state sample-stability estimates for finite-order SGK systems.

5.5. SGK-based numerical robustness and joint operating region

All operating regions in this subsection are numerical regions for the full $N = 8$ SGK stochastic system. At each of $\tau = 2.20, 2.35, 2.50$, three noise levels are selected below the P bracket, between the P bracket and D boundary, and above the D boundary. Twenty-four independent realizations are computed at each point from the corresponding deterministic rotating wave. Let $A(t) = 4^{-1} \sum_{j=1}^{4} |z_j(t)|$. The symbols $\bar{r}_c$ and $\bar{A}$ denote retained-sample means followed by ensemble averaging, CV_A is the corresponding amplitude coefficient of variation, and P_0 is the retained-sample fraction classified as near zero. Phase statistics are collected only when all four oscillator amplitudes exceed $\max(10^{-4}, 0.05R_{\mathrm{det},8})$. A realization is successful when the mean phase error is at most 0.15 rad, the near-zero fraction is at most 0.2, and the valid-phase fraction is at least 0.8. These are empirical numerical criteria adopted in this study. They limit phase deviation and near-zero occupancy while requiring phase information for at least 80% of the retained samples. They define the reported success classification, not the P-transition bracket or the D-boundary estimate. The resulting ensemble statistics are listed in Table 13.

Table 13. Stochastic quarter-cycle performance at sampled P–D points.

τ	σ	Region	$\bar{r}_c$	$\bar{A}$	CV_A	E_ϕ	P_0	Valid phase / successes
2.20	0.070	Inside P	0.0550	0.0367	0.312	0.0474	0.000	1.000 / 24/24
2.20	0.127	P–D transition	0.0371	0.0248	0.713	0.0833	0.081	0.890 / 20/24
2.20	0.170	Beyond D	0.0248	0.0166	1.078	0.1115	0.302	0.656 / 12/24
2.35	0.120	Inside P	0.0788	0.0524	0.412	0.0029	0.000	1.000 / 24/24
2.35	0.190	P–D transition	0.0442	0.0294	0.924	0.0047	0.200	0.740 / 15/24
2.35	0.250	Beyond D	0.0220	0.0146	1.488	0.0062	0.506	0.404 / 4/24
2.50	0.090	Inside P	0.0602	0.0400	0.374	0.0556	0.000	1.000 / 24/24
2.50	0.150	P–D transition	0.0382	0.0254	0.808	0.0900	0.131	0.814 / 15/24
2.50	0.200	Beyond D	0.0230	0.0153	1.244	0.1207	0.375	0.544 / 7/24

Note. Success is reported as an observed count out of 24 realizations. The exact 95% Clopper–Pearson intervals are [0.858,1.000] for 24/24, [0.626,0.953] for 20/24, [0.406,0.812] for 15/24, [0.291,0.709] for 12/24, [0.126,0.511] for 7/24, and [0.047,0.374] for 4/24.

Table 13 shows a systematic deterioration across the three regimes. All inside-P points have 100% success, the P–D points exhibit larger amplitude variability and near-zero occupancy, and the beyond-D points have success probabilities of only 16.7–50.0%. The exact binomial intervals remain broad for 24 realizations, so the success values are interpreted as sampled performance estimates rather than precise probabilities. The conditional phase error must be read together with the valid-phase fraction because phase is evaluated only on retained nonzero-amplitude samples.

Figure 9 maps these same nine simulations onto the P–D envelope diagram; panels (b)–(d) reuse the same coordinates so that success, phase error, and near-zero occupancy can be compared point by point.

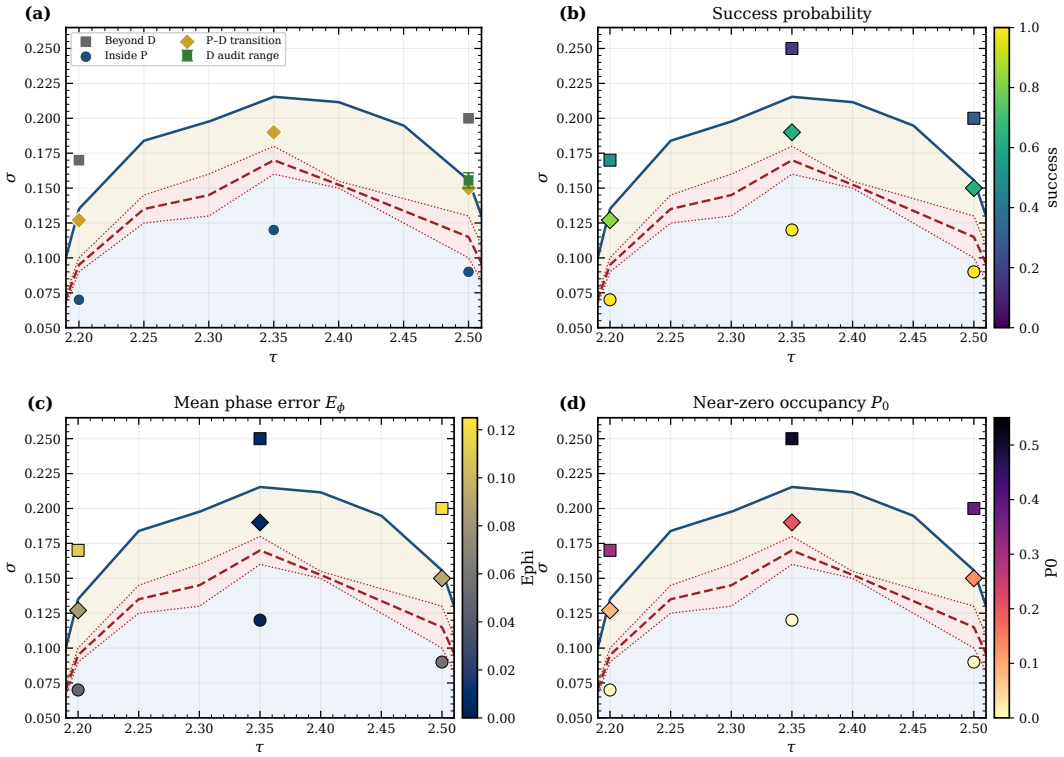


Figure 9. Full $N = 8$ SGK performance at nine sampled points: (a) P/D envelopes; (b) success probability; (c) mean phase error; (d) near-zero occupancy.

In Figure 9(a), the three marker classes separate the inside-P, intermediate P–D, and beyond-D regimes. Panels (b)–(d) show that the reduction in success is accompanied by increasing near-zero occupancy, whereas a small conditional phase error can persist after amplitude reliability has already degraded.

Representative single-realization diagnostics for the three $\tau = 2.35$ cases in Table 13 are shown in Figure 10. The columns correspond to $\sigma = 0.12$, 0.19, and 0.25, representing the inside-P, P–D-transition, and beyond-D regimes. The valid-phase annotations are trajectory-specific and are not the ensemble averages in Table 13. The phase-error curves must be interpreted jointly with the normalized amplitude traces and the final joint $(r_c/R_{\mathrm{det}}, E_\phi)$ distributions.

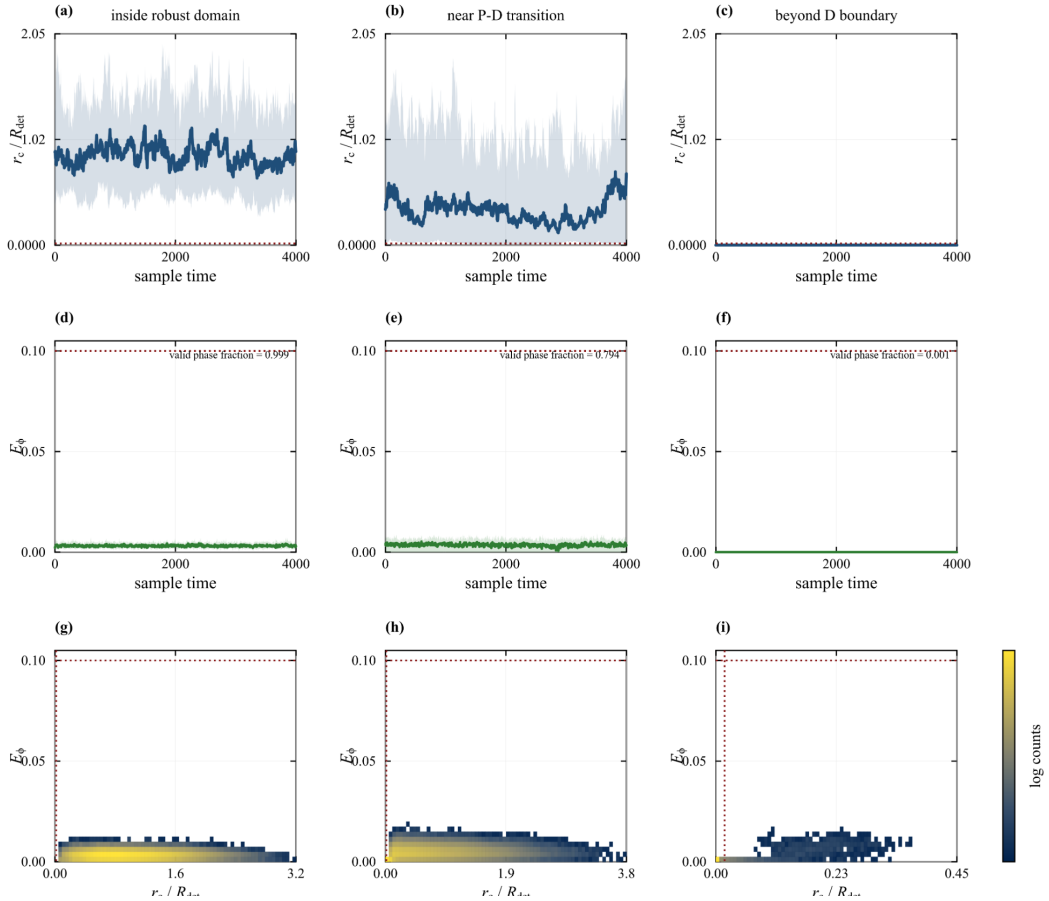


Figure 10. Single-realization diagnostics at $\tau = 2.35$ and $\sigma = 0.12, 0.19, 0.25$: normalized amplitude, phase error, and joint amplitude–phase distributions (top to bottom).

Figure 10 provides the trajectory-level mechanism behind the ensemble statistics. The normalized amplitude remains well separated from zero inside P, becomes intermittent near the P–D transition, and collapses beyond D. The corresponding joint distributions show why phase-only diagnostics are insufficient near the absorbing state.

For the six sampled P brackets, the lower, midpoint, and upper values are connected piecewise linearly. The D estimates are treated in the same way, using the independently audited $\tau = 2.50$ value. Zero-noise values are appended at the two deterministic SGK Hopf endpoints; these endpoint segments are model-based extrapolations rather than direct stochastic calculations. Table 14 therefore reports candidate P/D operating intervals, not continuously phase-validated quarter-cycle feasible intervals.

The displayed endpoints are interpolation outputs and are rounded to two decimal places to avoid implying unsupported statistical precision.

Table 14. Candidate SGK P–D operating intervals.

$\bar{\sigma}$	D-range	P envelope	Joint range	τ^*	Joint margin
0.08	(2.18, 2.53)	Lower	(2.20, 2.51)	2.35	0.08
		Midpoint	(2.19, 2.52)		0.09
		Upper	(2.19, 2.52)		0.10
0.12	(2.20, 2.51)	Lower	(2.24, 2.46)	2.35	0.04
		Midpoint	(2.23, 2.49)		0.05
		Upper	(2.22, 2.51)		0.06
0.15	(2.22, 2.50)	Lower	(2.33, 2.40)	2.35	0.01
		Midpoint	(2.31, 2.41)		0.02
		Upper	(2.27, 2.42)		0.03

Table 14 shows that the lower P envelope is the active constraint at all three prescribed noise levels. The midpoint and upper-envelope intervals indicate the finite-grid spread, while $\tau^* = 2.35$ gives the largest sampled lower-envelope margin. These are interpolation-based numerical summaries rather than globally optimized or continuously phase-validated engineering ranges. Figure 11 then relates the normalized distances and joint margins to the performance statistics measured at the nine sampled points.

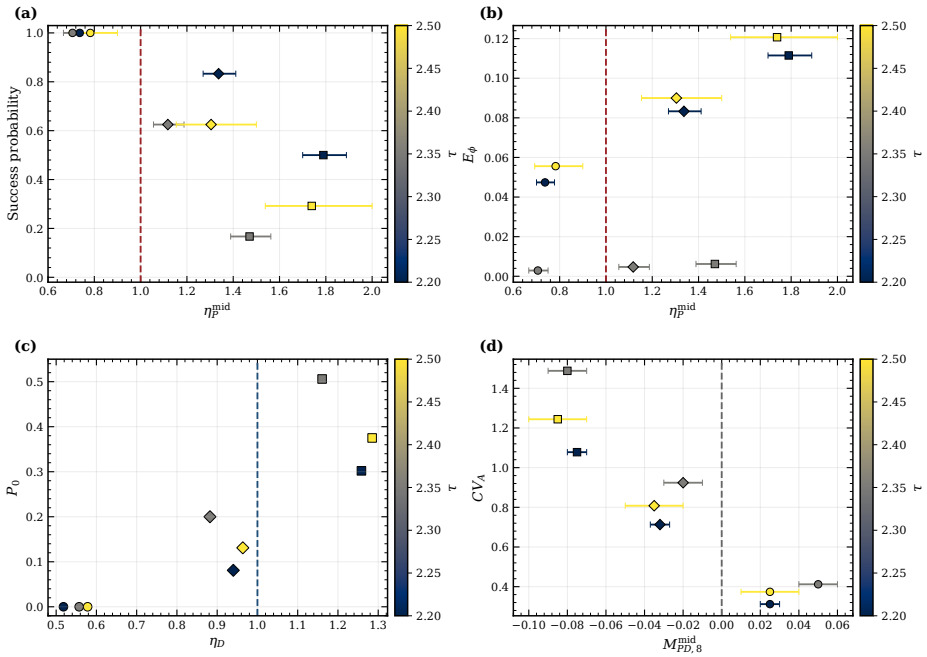


Figure 11. Dimensionless SGK performance: (a)–(b) success and phase error versus P distance; (c) near-zero occupancy versus D distance; (d) amplitude variability versus joint margin.

Horizontal bars in Figure 11 propagate P-bracket endpoints and are not confidence intervals. Figures 11(a) and (b) show that points beyond the midpoint P distance generally lose success before the

D distance changes sign, while panels (c) and (d) connect near-zero occupancy and amplitude variability to the D distance and joint margin. This comparison supports the use of the P bracket as the earlier operational warning.

The numerical P bracket is an early-warning range for probabilistic amplitude degradation, whereas the D boundary marks the later change in sample stability of the absorbing zero state. A point may remain below the D boundary while already lying beyond the P bracket and exhibiting reduced success. These conclusions apply to the full $N = 8$ SGK stochastic system. The $N = 9$ and $N = 10$ anchors support the direction of the density transition, but the remaining stationarity warnings and finite-grid uncertainty are retained in the reported envelopes. For the original infinite-dimensional stochastic delay equation, the results remain SGK-based numerical evidence rather than a complete stochastic bifurcation proof.

6. Conclusions

This study distinguishes the original deterministic DDE, the original infinite-dimensional stochastic delay equation, the full finite-order SGK stochastic system, and the auxiliary direct center-projection model. This separation prevents local projected indicators from being presented as exact stochastic boundaries of either the full SGK system or the original delay equation.

The original deterministic DDE selects the critical four-phase rotating-wave mode with adjacent phase differences of $\pi/2$ and validates its algebraic relation directly. The $N = 8$ SGK system is the lowest tested order used as the principal computational compromise for the stated left-Hopf and reconstruction diagnostics, but its right Hopf endpoint retains a 0.240% discrepancy relative to the direct DDE. Continuation gives the finite-order interval $I_{\mathrm{det}}^{(8)} = (2.1612, 2.5610)$, whose right endpoint is a reconnection with the equilibrium at a second Hopf point.

The auxiliary direct center-projection model explains why a P-type loss of the positive-amplitude density peak can precede the D-type stabilization of the absorbing state as noise increases. Because the noise channels generally do not preserve the deterministic center subspace, the projected formulas are retained only as local indicators. The final stochastic results are obtained from long-time simulations of the full $N = 8$ SGK stochastic system. At all six sampled delays, the numerical P-transition bracket lies below the D-boundary estimate. Representative $N = 9$ and $N = 10$ anchors preserve the same low-noise interior-peak and high-noise boundary-dominated classifications, but they do not locate complete high-order P brackets. At $\tau = 2.50$, the independent multi-seed D audit gives central $N = 8$ estimates near 0.155–0.156 and a conservative numerical range $[0.150, 0.161]$, showing that the previously reported values 0.1594 and 0.1598 were protocol-dependent higher estimates rather than two independent converged boundaries.

The lower, midpoint, and upper P-bracket envelopes quantify finite-grid uncertainty in candidate SGK P/D operating intervals. At prescribed noise levels 0.08, 0.12, and 0.15, the conservative joint intervals are approximately $(2.20, 2.51)$, $(2.24, 2.46)$, and $(2.33, 2.40)$, respectively, because the P lower envelope is the active constraint. On the present sampled delay grid, $\tau = 2.35$ gives the largest reported margin. This is a dimensionless sampled-grid numerical recommendation, not a global optimum or a robot-level engineering validation.

The complete P brackets, D-boundary estimates, and joint operating envelopes are numerical results for finite-dimensional SGK systems. For the original infinite-dimensional stochastic delay equation,

they provide evidence supported by deterministic DDE comparisons and SGK-order checks, but not a rigorous proof of its P- or D-bifurcation boundaries. Direct long-time SDDE validation and coupling with full quadruped-body and contact dynamics remain important extensions.

Appendix

A. Stochastic center projection and polar Itô transformation

A.1. Vanishing of the counter-rotating diffusion coefficients

For the auxiliary direct center-projection model, the projection of the jth diffusion channel onto the critical left eigendirection is

$$\boldsymbol{u}^* \boldsymbol{L}_j \boldsymbol{Y} = \gamma_j w + \delta_j \bar{w} + R_j(w, \bar{w}, \eta), \tag{A.1}$$

where $\gamma_j = \boldsymbol{u}^* \boldsymbol{L}_j \boldsymbol{v}$ and $\delta_j = \boldsymbol{u}^* \boldsymbol{L}_j \bar{\boldsymbol{v}}$, while $R_j(w, \bar{w}, \eta) = O(|w|^2 + |\eta||w|)$.

Introduce the blockwise complex-structure operators $\boldsymbol{J}_2 = \left[\begin{smallmatrix} 0 & -1 \\ 1 & 0 \end{smallmatrix}\right]$, $\boldsymbol{J}_8 = \boldsymbol{I}_4 \otimes \boldsymbol{J}_2$, and $\boldsymbol{\mathcal{J}}_N = \boldsymbol{I}_N \otimes \boldsymbol{J}_8$.

The block structures of the SGK drift matrix and the diffusion-channel operators imply

$$\boldsymbol{A}_{\mathrm{SGK}}(\tau)\boldsymbol{\mathcal{J}}_N = \boldsymbol{\mathcal{J}}_N \boldsymbol{A}_{\mathrm{SGK}}(\tau), \qquad \boldsymbol{L}_j \boldsymbol{\mathcal{J}}_N = \boldsymbol{\mathcal{J}}_N \boldsymbol{L}_j, \qquad j = 1, \ldots, 4. \tag{A.2}$$

Therefore, the critical right and left eigenvectors can be selected with positive-rotation polarization:

$$\boldsymbol{\mathcal{J}}_N \boldsymbol{v} = \mathrm{i}\boldsymbol{v}, \qquad \boldsymbol{\mathcal{J}}_N \boldsymbol{u} = \mathrm{i}\boldsymbol{u}. \tag{A.3}$$

Since the blockwise complex-structure operator is real, complex conjugation of the first relation in Eq (A.3) gives $\boldsymbol{\mathcal{J}}_N \bar{\boldsymbol{v}} = -\mathrm{i}\bar{\boldsymbol{v}}$.

Using the commutation relation in Eq (A.2), it follows that

$$\boldsymbol{\mathcal{J}}_N \boldsymbol{L}_j \bar{\boldsymbol{v}} = \boldsymbol{L}_j \boldsymbol{\mathcal{J}}_N \bar{\boldsymbol{v}} = -\mathrm{i}\boldsymbol{L}_j \bar{\boldsymbol{v}}. \tag{A.4}$$

Moreover, the blockwise complex-structure operator is skew-Hermitian:

$$\boldsymbol{\mathcal{J}}_N^* = -\boldsymbol{\mathcal{J}}_N. \tag{A.5}$$

On the one hand, the second relation in Eq (A.3) yields

$$(\boldsymbol{\mathcal{J}}_N \boldsymbol{u})^* \boldsymbol{L}_j \bar{\boldsymbol{v}} = (\mathrm{i}\boldsymbol{u})^* \boldsymbol{L}_j \bar{\boldsymbol{v}} = -\mathrm{i}\boldsymbol{u}^* \boldsymbol{L}_j \bar{\boldsymbol{v}}. \tag{A.6}$$

On the other hand, Eqs (A.4) and (A.5) give

$$(\boldsymbol{\mathcal{J}}_N \boldsymbol{u})^* \boldsymbol{L}_j \bar{\boldsymbol{v}} = \boldsymbol{u}^* \boldsymbol{\mathcal{J}}_N^* \boldsymbol{L}_j \bar{\boldsymbol{v}} = -\boldsymbol{u}^* \boldsymbol{\mathcal{J}}_N \boldsymbol{L}_j \bar{\boldsymbol{v}} = \mathrm{i}\boldsymbol{u}^* \boldsymbol{L}_j \bar{\boldsymbol{v}}. \tag{A.7}$$

Comparison of Eqs (A.6) and (A.7) gives $\boldsymbol{u}^* \boldsymbol{L}_j \bar{\boldsymbol{v}} = 0$. Consequently, $\delta_j = 0$ for $j = 1, \ldots, 4$, and Eq (A.1) reduces to $\boldsymbol{u}^* \boldsymbol{L}_j \boldsymbol{Y} = \gamma_j w + R_j(w, \bar{w}, \eta)$.

Neglecting the higher-order stochastic remainder terms gives the truncated stochastic center equation

$$\mathrm{d}w = \left[(\beta + \mathrm{i}\Omega(\tau))w + c_H w|w|^2\right]\mathrm{d}t + \sigma w \sum_{j=1}^{4} \gamma_j \, \mathrm{d}W_j(t). \tag{A.8}$$

A.2. Polar Itô transformation

Write $w = x + \mathrm{i}y = r\exp(\mathrm{i}\theta)$, $c_H = a + \mathrm{i}b$, and $\gamma_j = \gamma_{jR} + \mathrm{i}\gamma_{jI}$.
The real and imaginary parts of Eq (A.8) satisfy

$$\mathrm{d}x = \Big[(\beta + ar^2)x - (\Omega(\tau) + br^2)y\Big]\mathrm{d}t + \sigma \sum_{j=1}^{4}(\gamma_{jR}x - \gamma_{jI}y)\mathrm{d}W_j(t), \tag{A.9}$$

and

$$\mathrm{d}y = \Big[(\Omega(\tau) + br^2)x + (\beta + ar^2)y\Big]\mathrm{d}t + \sigma \sum_{j=1}^{4}(\gamma_{jI}x + \gamma_{jR}y)\mathrm{d}W_j(t). \tag{A.10}$$

Define the deterministic drift and the jth diffusion vector by

$$\begin{aligned} \boldsymbol{f}(x,y) &= \mathrm{col}((\beta + ar^2)x - (\Omega(\tau) + br^2)y,\ (\Omega(\tau) + br^2)x + (\beta + ar^2)y), \\ \boldsymbol{g}_j(x,y) &= \mathrm{col}(\gamma_{jR}x - \gamma_{jI}y,\ \gamma_{jI}x + \gamma_{jR}y). \end{aligned} \tag{A.11}$$

For $r > 0$, Itô's formula applied to the radial coordinate gives

$$\mathrm{d}r = \left[\nabla r \cdot \boldsymbol{f} + \frac{\sigma^2}{2}\sum_{j=1}^{4}\boldsymbol{g}_j^{\mathsf{T}} D^2 r\, \boldsymbol{g}_j\right]\mathrm{d}t + \sigma\sum_{j=1}^{4}\nabla r \cdot \boldsymbol{g}_j\,\mathrm{d}W_j(t). \tag{A.12}$$

The gradient and Hessian of r are $\nabla r = r^{-1}\,\mathrm{col}(x,y)$ and $D^2 r = r^{-3}\left[\begin{smallmatrix} y^2 & -xy \\ -xy & x^2 \end{smallmatrix}\right]$, respectively.
The deterministic contribution satisfies

$$\nabla r \cdot \boldsymbol{f} = \frac{x}{r}\Big[(\beta + ar^2)x - (\Omega(\tau) + br^2)y\Big] + \frac{y}{r}\Big[(\Omega(\tau) + br^2)x + (\beta + ar^2)y\Big] = (\beta + ar^2)r. \tag{A.13}$$

For the jth diffusion channel,

$$\nabla r \cdot \boldsymbol{g}_j = \frac{x(\gamma_{jR}x - \gamma_{jI}y) + y(\gamma_{jI}x + \gamma_{jR}y)}{r} = \gamma_{jR}r. \tag{A.14}$$

The corresponding second-order Itô contribution is

$$\boldsymbol{g}_j^{\mathsf{T}} D^2 r\, \boldsymbol{g}_j = \frac{1}{r^3}\Big[y(\gamma_{jR}x - \gamma_{jI}y) - x(\gamma_{jI}x + \gamma_{jR}y)\Big]^2 = \gamma_{jI}^2 r. \tag{A.15}$$

Substituting Eqs (A.13)–(A.15) into Eq (A.12) yields

$$\mathrm{d}r = \left[\left(\beta + \frac{\sigma^2}{2}\sum_{j=1}^{4}\gamma_{jI}^2\right)r + ar^3\right]\mathrm{d}t + \sigma r\sum_{j=1}^{4}\gamma_{jR}\,\mathrm{d}W_j(t). \tag{A.16}$$

For the phase variable $\theta(x,y) = \arg(x + \mathrm{i}y)$, Itô's formula gives

$$\mathrm{d}\theta = \left[\nabla\theta \cdot \boldsymbol{f} + \frac{\sigma^2}{2}\sum_{j=1}^{4}\boldsymbol{g}_j^{\mathsf{T}} D^2\theta\, \boldsymbol{g}_j\right]\mathrm{d}t + \sigma\sum_{j=1}^{4}\nabla\theta \cdot \boldsymbol{g}_j\,\mathrm{d}W_j(t). \tag{A.17}$$

The gradient and Hessian of θ are

$$\nabla\theta = \frac{1}{r^2}\begin{bmatrix} -y \\ x \end{bmatrix}, \qquad D^2\theta = \frac{1}{r^4}\begin{bmatrix} 2xy & y^2 - x^2 \\ y^2 - x^2 & -2xy \end{bmatrix}. \tag{A.18}$$

The deterministic part satisfies

$$\nabla\theta \cdot \boldsymbol{f} = -\frac{y}{r^2}\Big[(\beta + ar^2)x - (\Omega(\tau) + br^2)y\Big] + \frac{x}{r^2}\Big[(\Omega(\tau) + br^2)x + (\beta + ar^2)y\Big] = \Omega(\tau) + br^2. \tag{A.19}$$

For the jth diffusion channel,

$$\nabla\theta \cdot \boldsymbol{g}_j = \frac{1}{r^2}\Big[-y(\gamma_{jR}x - \gamma_{jI}y) + x(\gamma_{jI}x + \gamma_{jR}y)\Big] = \gamma_{jI}. \tag{A.20}$$

A direct calculation of the second-order term gives

$$\boldsymbol{g}_j^{\mathsf{T}} D^2\theta\, \boldsymbol{g}_j = -2\gamma_{jR}\gamma_{jI}. \tag{A.21}$$

Substitution of Eqs (A.19)–(A.21) into Eq (A.17) gives

$$\mathrm{d}\theta = \left[\Omega(\tau) + br^2 - \sigma^2 \sum_{j=1}^{4} \gamma_{jR}\gamma_{jI}\right]\mathrm{d}t + \sigma \sum_{j=1}^{4} \gamma_{jI}\,\mathrm{d}W_j(t). \tag{A.22}$$

Using the coefficient definitions

$$q_r = \sum_{j=1}^{4} \gamma_{jR}^2, \qquad q_\theta = \sum_{j=1}^{4} \gamma_{jI}^2, \tag{A.23}$$

and

$$\kappa_r = \frac{1}{2}q_\theta, \qquad \kappa_\theta = -\sum_{j=1}^{4} \gamma_{jR}\gamma_{jI}, \tag{A.24}$$

the polar stochastic equations become

$$\mathrm{d}r = \Big[(\beta + \sigma^2\kappa_r)r + ar^3\Big]\mathrm{d}t + \sigma r \sum_{j=1}^{4} \gamma_{jR}\,\mathrm{d}W_j(t), \tag{A.25}$$

and

$$\mathrm{d}\theta = \Big[\Omega(\tau) + br^2 + \sigma^2\kappa_\theta\Big]\mathrm{d}t + \sigma \sum_{j=1}^{4} \gamma_{jI}\,\mathrm{d}W_j(t). \tag{A.26}$$

For $q_r > 0$, define

$$B_r(t) = \frac{1}{\sqrt{q_r}} \sum_{j=1}^{4} \gamma_{jR} W_j(t). \tag{A.27}$$

Since $W_1, \ldots, W_4$ are mutually independent,

$$\langle B_r \rangle_t = \frac{1}{q_r} \sum_{j=1}^{4} \gamma_{jR}^2 t = t. \tag{A.28}$$

Thus, $B_r(t)$ is a standard real-valued Wiener process, and Eq (A.25) can be written as

$$\mathrm{d}r = \left[(\beta + \sigma^2 \kappa_r) r + a r^3\right] \mathrm{d}t + \sigma \sqrt{q_r}\, r\, \mathrm{d}B_r(t). \tag{A.29}$$

Author contributions

Qiyuan He: Conceptualization, methodology, software, formal analysis, investigation, validation, visualization, writing–original draft, writing–review and editing; Chonghe Shi: Visualization, writing–review and editing; Zikun Han: Investigation, validation, visualization; Qiubao Wang: Conceptualization, methodology, resources, funding acquisition, supervision, writing–review and editing. All authors have read and approved the final version of the manuscript.

Use of generative-AI tools declaration

During the preparation of this manuscript, the authors used ChatGPT (OpenAI) to assist with English translation and language editing, LaTeX formatting, and figure presentation. All AI-assisted content was reviewed and revised by the authors. The authors verified the mathematical derivations, numerical computations, data interpretation, and final manuscript and take full responsibility for the published content.

Acknowledgments

This work was supported by the National Natural Science Foundation of China (Nos. 11602151 and 11872253), the 2026 Graduate Curriculum Ideological and Political Education Demonstration Project of the Hebei Provincial Department of Education (No. YKCSZ2026040), and the 2026 College Student Innovation and Entrepreneurship Training Program (No. 202610107036).

Conflict of interest

All authors declare no conflicts of interest in this paper.

References

1. P. Holmes, R. J. Full, D. E. Koditschek, J. Guckenheimer, The dynamics of legged locomotion: Models, analyses, and challenges, *SIAM Rev.*, **48** (2006), 207–304. https://doi.org/10.1137/S0036144504445133
2. A. J. Ijspeert, Central pattern generators for locomotion control in animals and robots: A review, *Neural Netw.*, **21** (2008), 642–653. https://doi.org/10.1016/j.neunet.2008.03.014

3. J. J. Collins, I. N. Stewart, Coupled nonlinear oscillators and the symmetries of animal gaits, *J. Nonlinear Sci.*, **3** (1993), 349–392. https://doi.org/10.1007/BF02429870
4. C. P. Santos, V. Matos, Gait transition and modulation in a quadruped robot: A brainstem-like modulation approach, *Robot. Auton. Syst.*, **59** (2011), 620–634. https://doi.org/10.1016/j.robot.2011.05.003
5. J. Buchli, A. J. Ijspeert, Self-organized adaptive legged locomotion in a compliant quadruped robot, *Auton. Robots*, **25** (2008), 331–347. https://doi.org/10.1007/s10514-008-9099-2
6. I. Stewart, Spontaneous symmetry-breaking in a network model for quadruped locomotion, *Int. J. Bifurcation Chaos*, **27** (2017), 1730049. https://doi.org/10.1142/S021812741730049X
7. Z. Aminzare, V. Srivastava, P. Holmes, Gait transitions in a phase oscillator model of an insect central pattern generator, *SIAM J. Appl. Dyn. Syst.*, **17** (2018), 626–671. https://doi.org/10.1137/17M1125571
8. Z. Song, X. Huang, J. Xu, Spatiotemporal pattern of periodic rhythms in delayed Van der Pol oscillators for the CPG-based locomotion of snake-like robot, *Nonlinear Dyn.*, **110** (2022), 3377–3393. https://doi.org/10.1007/s11071-022-07783-y
9. Z. Song, J. Zhu, J. Xu, Gaits generation of quadruped locomotion for the CPG controller by the delay-coupled VDP oscillators, *Nonlinear Dyn.*, **111** (2023), 18461–18479. https://doi.org/10.1007/s11071-023-08783-2
10. X. Yu, Z. Song, X. Sun, J. Xu, A theoretical approach for gait generation of the CPG controller by using the time-delay coupled oscillators, *SIAM J. Appl. Dyn. Syst.*, **25** (2026), 518–553. https://doi.org/10.1137/25M1739820
11. H. Li, Y. Tian, T. Huang, P. Yang, Hopf bifurcation and hybrid control of a delayed diffusive semi-ratio-dependent predator–prey model, *AIMS Math.*, **9** (2024), 29608–29632. https://doi.org/10.3934/math.20241434
12. P. H. Baxendale, A stochastic Hopf bifurcation, *Probab. Theory Relat. Fields*, **99** (1994), 581–616. https://doi.org/10.1007/BF01206233
13. S. Hussain, T. N. Alharthi, Bifurcation and persistence in a stochastic seasonal dynamical system, *AIMS Math.*, **11** (2026), 13126–13148. https://doi.org/10.3934/math.2026541
14. M. Gaudreault, F. Lépine, J. Viñals, Pitchfork and Hopf bifurcation thresholds in stochastic equations with delayed feedback, *Phys. Rev. E*, **80** (2009), 061920. https://doi.org/10.1103/PhysRevE.80.061920
15. Y. Yang, Q. Wang, Capture of stochastic P-bifurcation in a delayed mechanical centrifugal governor, *Chaos Soliton. Fract.*, **174** (2023), 113910. https://doi.org/10.1016/j.chaos.2023.113910
16. M. D. Chekroun, I. Koren, H. Liu, H. Liu, Generic generation of noise-driven chaos in stochastic time delay systems: Bridging the gap with high-end simulations, *Sci. Adv.*, **8** (2022), eabq7137. https://doi.org/10.1126/sciadv.abq7137
17. Z. Han, Q. Wang, H. Wu, Z. Hu, Stochastic P-bifurcation in a delayed Myc/E2F/miR-17-92 network, *Int. J. Bifurcation Chaos*, **32** (2022), 2250159. https://doi.org/10.1142/S0218127422501590

18. Q. Wang, Z. Han, X. Zhang, Y. Yang, Dynamics of the delay-coupled bubble system combined with the stochastic term, *Chaos Soliton. Fract.*, **148** (2021), 111053. https://doi.org/10.1016/j.chaos.2021.111053

19. Z. Hu, Z. Han, Y. Yang, Q. Wang, Combined impact of multidelay feedback number and interval: A novel mechanism for controlling the stability of stochastic Duffing systems, *Int. J. Bifurcation Chaos*, **34** (2024), 2450108. https://doi.org/10.1142/S0218127424501086

20. N. Zhang, Z. Wang, J. H. Park, W. Li, Semi-global synchronization of stochastic mixed time-delay systems with Lévy Noise under aperiodic intermittent delayed sampled-data control, *Automatica*, **171** (2025), 111963. https://doi.org/10.1016/j.automatica.2024.111963

21. N. Zhang, Q. Hu, J. H. Park, W. Li, Exponential stability of stochastic highly nonlinear delayed systems with regime-switching diffusion under asynchronous intermittent control, *IEEE Trans. Autom. Control*, **70** (2025), 8375–8381. https://doi.org/10.1109/TAC.2025.3583609

22. N. Zhang, X. Wang, W. Li, Stability for multi-linked stochastic delayed complex networks with stochastic hybrid impulses by Dupire Itô's formula, *Nonlinear Anal. Hybrid Syst.*, **45** (2022), 101200. https://doi.org/10.1016/j.nahs.2022.101200

23. M. D. Chekroun, M. Ghil, H. Liu, S. Wang, Low-dimensional Galerkin approximations of nonlinear delay differential equations, *Discrete Contin. Dyn. Syst.*, **36** (2016), 4133–4177. https://doi.org/10.3934/dcds.2016.36.4133

24. M. D. Chekroun, H. Liu, Effective reduced models from delay differential equations: Bifurcations, tipping solution paths, and ENSO variability, *Physica D*, **460** (2024), 134058. https://doi.org/10.1016/j.physd.2024.134058

25. Z. Liu, Z. Han, J. Xu, Q. Wang, Stochastic Galerkin–Koornwinder method on analyzing stochastic MEMS gyroscope with time delay feedback control, *J. Comput. Appl. Math.*, **483** (2026), 117396. https://doi.org/10.1016/j.cam.2026.117396

26. G. Fodor, H. T. Sykora, D. Bachrathy, Collocation method for stochastic delay differential equations, *Probab. Eng. Mech.*, **74** (2023), 103515. https://doi.org/10.1016/j.probengmech.2023.103515

27. Y. Zhang, Y. Jin, P. Xu, S. Xiao, Stochastic bifurcations in a nonlinear tri-stable energy harvester under colored noise, *Nonlinear Dyn.*, **99** (2020), 879–897. https://doi.org/10.1007/s11071-018-4702-3

28. Y. H. Sun, Y. G. Yang, W. Xu, Stochastic P-bifurcations of a noisy nonlinear system with fractional derivative element, *Acta Mech. Sin.*, **37** (2021), 507–515. https://doi.org/10.1007/s10409-020-01020-8



AIMS Press

© 2026 the Author(s), licensee AIMS Press. This is an open access article distributed under the terms of the Creative Commons Attribution License (http://creativecommons.org/licenses/by/4.0)